Diploma Thesis

Numerical Comparison of the Flow through an Axial Turbine Row: Linear Cascade vs. Annular Cascade

Aleksander Adam Makaruk
Matriculation number: 106091

Written under the direction of:

dr inż. Ryszard Chodkiewicz

Technical University of Łódź,
Faculty of Mechanical Engineering,
Institute of Turbomachinery.

Univ.Ass.Dipl.-Ing.Dr.techn.
Franz Wingelhofer
&
Ao.Univ.Prof. Dipl.-Ing. Dr.techn.
Reinhard Willinger

Vienna University of Technology,
Institute of Thermodynamics and
Energy Conversion.

Vienna 2005

Abstract

The method of Computational Fluid Dynamics was used to investigate the differences in the flow between a linear cascade and annular cascades of various hub-to-tip ratios. The experiments were performed on models deriving from a stator of a high-pressure turbine.

It was found that phenomena like secondary velocities or losses intensify near the hub and diminish near the shroud of a cascade as the hub-to-tip ratio decreases. Moreover, the outlet angle experiences underturning near the hub and overturning near the shroud for the decreasing hub-to-tip ratios.

Keywords: linear cascade, annular cascade, hub-to-tip ratio, flow turning, flow asymmetry.

Acknowledgements

I would like to thank my supervisors Dr. Franz Wingelhofer and Dr. Ryszard Chodkiewicz for their useful suggestions and leading when I was writing this thesis.

I wish also to thank for the appreciated support that I received from Dr. Krzysztof Jóźwik and Dr. Reinhard Willinger for giving me the possibility to write the thesis at ITE.

I would like to dedicate this thesis to my parents.

Nomenclature

Latin symbols:

a	velocity of sound	m/s
A_o	area of the opening	m^2
b	axial chord length	m
c	chord length	m
c	velocity	m/s
cmp	vector component	1
Cp	specific heat capacity at constant pressure	$m^2/(s^2K)$
D_H	hydraulic diameter	m
I	turbulence intensity	1
h	span	m
k	exponent for description of boundary layer	1
k	turbulent kinetic energy	m^2/s^2
$LKEL$	local kinetic energy loss	1
M	Mach number	1
n	blade number	1
o	throat width	m
p	pressure	$kg/(ms^2)$
Q_{EAS}	“EquiAngle Skew”	1

r	radius	m
R	gas constant	$m^2/(s^2K)$
Re	Reynolds number	1
s	pitch	m
S_o	circumference of the opening	m
T	temperature	K
x	X-coordinate	m
y	Y-coordinate	m
Y	total pressure loss coefficient	1
y^+	dimensionless wall distance	1
z	Z-coordinate	m

Greek symbols:

β	flow angle	rad
δ	boundary layer thickness	m
$\delta*$	boundary layer displacement thickness	m
$\delta**$	boundary layer momentum thickness	m
ε	turbulent dissipation rate	m^2/s^3
ζ	enthalpy loss coefficient	1
θ	azimuth angle	rad
κ	ratio of the specific heat capacities	1
λ	turbulence length scale	m
ν	kinematic viscosity	m^2/s
ξ	vorticity	rad/s
ρ	density	kg/m^3
Φ	mass flux	$kg/(m^2s)$

Subscripts:

1	inlet or upstream
2	outlet or downstream
avg	average
h	hub
m	mean
MS	midspan
o	opening
prim	primary
proj	secondary projected
s	isentropic
sec	secondary
stream	streamwise
t	tip
t	total
u	circumferential
x	in the *X*-direction
XY	on the *XY*-plane
y	in the *Y*-direction
YZ	on the *YZ*-plane
z	in the *Z*-direction
∞	free stream
(x,y,z)	at the point *(x,y,z)*
δ	at the distance δ

Superscripts:

$\bar{}$	pitchwise averaged
^{ann}	annular
^{I}	design
^{I}	fluctuating

Abbreviations:

CFD	computational fluid dynamics
RMS	root-mean-square
UDF	user-defined function

Contents

1 Introduction

Even efficiency improvements by a fraction of percent lead to considerable gains in the power output of turbines. Simultaneously, they lead to a reduction of the costs of operation. In the energy production industry, hundreds of dollars or euros of an everyday saving multiplied by thousands of days of operation can result in immense amounts of money. In the aerospace industry, better efficiency causes overall advancement in the performance of an aircraft.

Mainly by the reasons given above, a great number of studies and experiments was performed in order to enhance the efficiency of turbomachines and to understand the loss creation phenomena, which can be seen in [1], [8], [13] to [19] and many other documents and books that were not included in the bibliography.

The behaviour of the flow through axial turbine bladings is usually investigated in wind tunnels. The annular arrangement of a turbine blade row is often simplified by the linear arrangement, which results in easier performance and in lower costs of the measurements. Due to that fact, some systematic errors are expected when turbine blades adapted in linear cascades are applied in real turbomachines. The examination of the differences caused by the annularity is the main aim of this diploma thesis. For this purpose, the method of Computational Fluid Dynamics was utilised. A model of a linear cascade and five models of annular cascades of various hub-to-tip ratios were built by means of the program GAMBIT. The flow through the cascades was simulated using a commercial CFD code, namely FLUENT. Boundary conditions as well as the geometries of the blade row were sourced from [1]. The turbulence of the flow was modelled by the standard k-ε turbulence model. The standard wall function was applied. The flow was simulated as steady. Isentropic Mach number distribution, outlet angle, local kinetic energy loss, streamwise vorticity, secondary velocity vectors and some other methods were chosen for the flow investigation. In most cases, flow characteristics were measured on a plane downstream. It was required to create some user-defined functions and custom field functions for pre- and postprocessing.

In Chapter 2, the original geometry and the calculation of the models' geometries together with the methods of the mesh construction are described. In addition, this section focuses on the mesh quality. The derivation of the data of the boundary conditions that were required as the input in FLUENT is presented in Chapter 3. Chapter 4 describes shortly the methods of the flow solution that were used. Chapter 5 concentrates on the description of the techniques that were applied to investigate the differences in the flow between the linear cascade and the annular cascades. Chapter 6 presents the results of the CFD simulation, and Chapter 7, the conclusions. In the appendices, the coordinates of the blade profile and codes of the UDF's with short descriptions are included.

2 Geometries & Meshes

2.1 Original Geometry

The geometry of a stator blade row from a high-pressure steam turbine was used for the investigation. It was sourced from the experiment described in [1]. The blade row is characterised by a high turning angle ($\Delta\beta^I = 89.4°$), by a low aspect ratio ($h/b = 1.47$) and by a relatively thick leading edge. The sketch and the essential details of the original blade row geometry are provided in Figure 1 and Table 1.

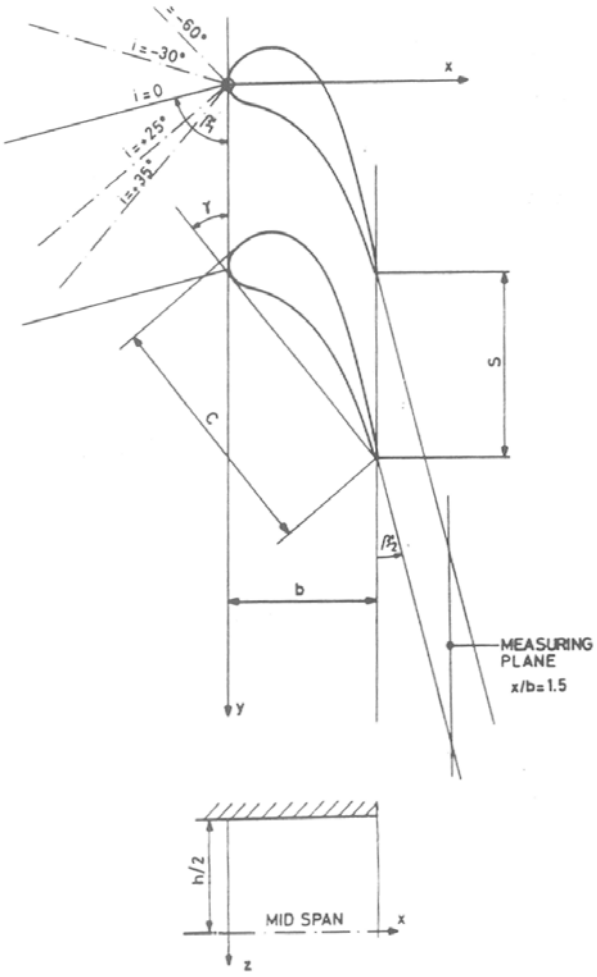

Figure 1 *- Cascade geometry [1]*

Table 1 *- Cascade geometry data*

Chord length, c	55.2mm
Axial chord length, b	34.0mm
Inlet blade angle, β^{I}_{1}	76.1°
Outlet blade angle, β^{I}_{2}	14.5°
Pitch, s	40.3mm
Span, h	50.0mm

Owing to the high turning angle, the cascade will be prone to produce high profile losses. The secondary losses are suspected to play an important role in the total loss of the cascade due to the low aspect ratio and the high turning angle [3].

2.2 2D Cascade

A 2D mesh was constructed for the purpose of checking the correctness of the midspan flow and adjusting the dimensionless wall distance. Moreover, it was used as the pattern for the 3D meshes. The geometry of the cascade was provided in the form of a set of coordinates and imported into GAMBIT. The set of coordinates can be found in Appendix B. The imported points were subsequently connected with the help of NURBS lines [5]. The inlet and the outlet of the computational domain were moved away with the distance of one and a half of the axial chord from the leading and trailing edge respectively.

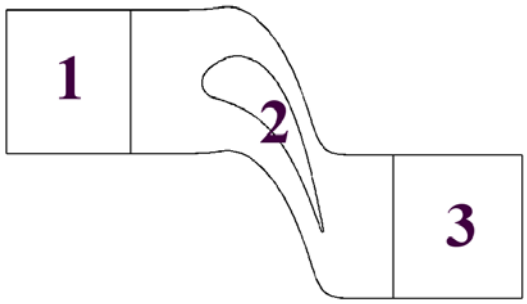

Figure 2 *- Regions of the 2D mesh*

The surfaces of the periodic boundary conditions were constructed from the middle line of the blade and connected smoothly to the inlet and outlet walls. The domain of the flow was divided into three regions as visualised in Figure 2. In the beginning, the edges were meshed in such a manner that the size of the elements was decreased in the spots where high pressure and high velocity gradients were expected. Special functions were applied around the blade to control the height of the cells in the vicinity of the walls. In Regions 1 and 3, structured meshes were used, resulting in the regular, quadrilateral form of the elements. In Region 2 a hybrid mesh, consisting of a structured O-type mesh around the blade and of an unstructured mesh, was employed. Several iterations were done till the dimensionless wall distance was in an acceptable range. For the final mesh, the dimensionless wall distance y^+ was in the range between *58* and *189*. Figure 3 presents the final outcome.

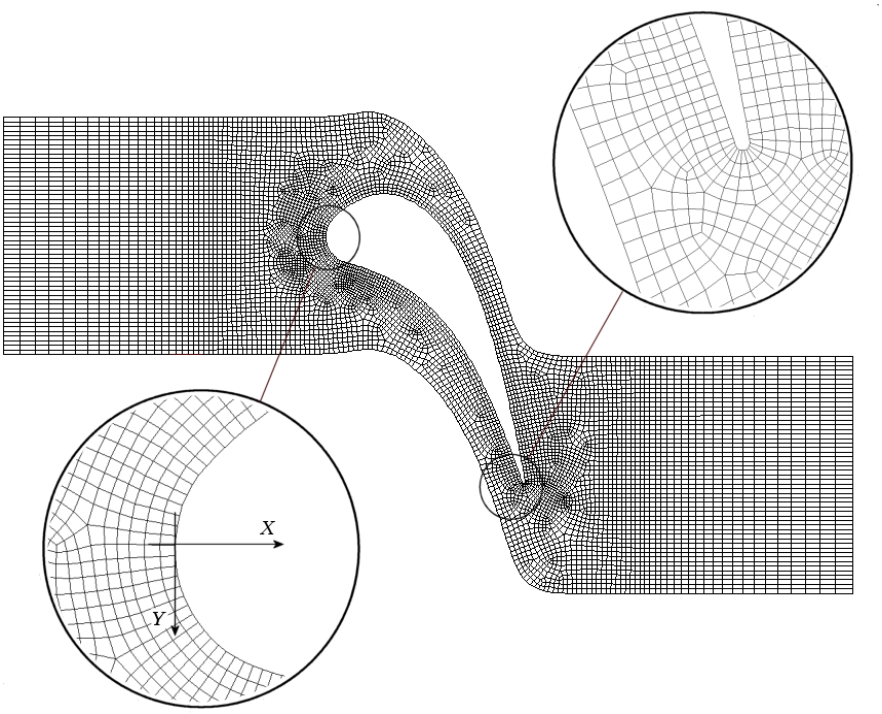

Figure 3 *– 2D mesh of the blade row*

A high mesh quality is crucial for adequate results of a CFD simulation. For the mesh used here is prone to a higher skewness rather than to a higher aspect ratio, the mesh quality was investigated only by means of the function called "EquiAngle Skew" [5], which is defined by

$$Q_{EAS} = \max\left(\frac{\theta_{\max} - 90°}{90°}, \frac{90° - \theta_{\min}}{90°}\right). \qquad (2.1)$$

The notations $\theta_{\min}$ and $\theta_{\max}$ are the minimum and maximum angles between two edges in an element. Usually, a mesh having "EquiAngle Skew" smaller than *0.5* is said to be of good quality, whereas it should not exceed *0.85* since such a mesh is likely to produce inaccurate results and slow the convergence [5].

The 2D mesh is formed of *7442* quadrilateral elements. Above *84 %* of the mesh cells possess values of the "EquiAngle Skew" lower than *0.1*. The highest value of the "EquiAngle Skew" of a cell in this mesh is *0.51*. According to the methods of the quality judgement [5], the mesh (presented above) is of high quality. The coordinate system was oriented in such a way that the *X*-axis indicates the direction of the flow upstream and the *Y*-axis is in agreement with the azimuthal component of the flow downstream of the cascade. The coordinate system was placed at the leading edge of the blade.

2.3 Linear Cascade

The model of the linear cascade exactly corresponds to one of the blade rows used in the experiment [1]. The 2D mesh was used as a base and was extruded along the span height with the distance $h=50mm$. The spanwise edges division was condensed in the regions close to the walls. The result is shown in Figure 4.

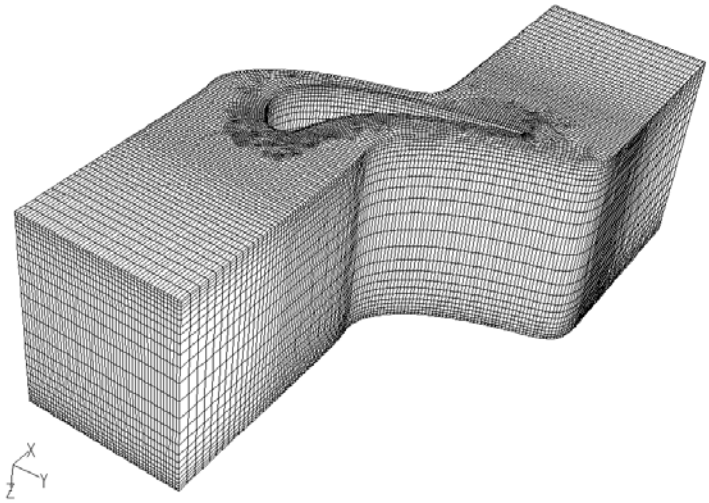

Figure 4 - *3D mesh of the linear cascade*

Since the extrusion was performed without any twist, the 3D mesh of the linear cascade preserves the quality achieved in the 2D mesh. The mesh is built of *178608* hexahedral cells. The coordinate system was oriented in the same manner as in case of the 2D mesh and placed on one of the end walls.

2.4 Annular Cascades

The geometries of five different annular cascades were calculated for five different hub-to-tip ratios r_h/r_t , which were assigned values: *0.975, 0.95, 0.9, 0.8,* and *0.7*. The mean radius r_m was defined to be a distance from the centre of rotation that divides the flow area between the hub and the casing in two areas of the same size. The mean radius can be obtained from the hub and the tip radius from

$$r_m = \sqrt{\frac{(r_h^2 + r_t^2)}{2}}. \qquad (2.2)$$

The blade number of an annular cascade is chosen in such a way that the azimuthal distance of two adjacent blades at the mean radius has the value of the pitch of the linear cascade:

$$n = \frac{2\pi r_m}{s}. \qquad (2.3)$$

The values of n were rounded to integer and the hub, the tip and the mean radii were calculated from (2.2) and (2.3) again. The resulting hub-to-tip ratios differed from the primal values. The differences, however, were small enough to assume them equal to *0.975, 0.95* etc. The results of the calculations and the characteristics of all cascades are given in Table 2. Other essential geometrical data are provided in Table 1.

Table 2 *– Cascades geometry data*

Cascade notation	*Linear*	K_A	K_B	K_C	K_D	K_E
Hub-to-tip ratio, r_h / r_t	*1*	*0.975*	*0.95*	*0.9*	*0.8*	*0.7*
Blade number, n	∞	*308*	*152*	*74*	*35*	*22*
Hub radius, r_h [mm]	∞	*1950.1*	*949.5*	*448.9*	*198.1*	*113.9*
Mean radius, r_m [mm]	∞	*1975.2*	*974.8*	*474.6*	*224.5*	*141.1*

Table 3 *– Approximate hub-to-tip ratios of the first stator rows of various turbines from [2]*

Turbine	r_h / r_t
Turbojet, Armstrong-Siddeley-Sapphire, *50 000 N*	*0.75*
Gas turbine, Allis Chalmers, *7 500 kW*	*0.78*
Warship gas turbine, Rolls-Royce, *4030 kW*	*0.79*
Gas turbine, -, *3300 kW*	*0.83*
Steam turbine of a nuclear power plant, -, *600 MW*	*0.83*
Low-power gas turbine, -, *350 kW*	*0.84*
Condensing turbine, Escher-Wyss-Oerlikon, *600 MW*	*0.86*
Back-pressure turbine, AEG, *5 000 kW*	*0.88*
Steam top-load turbine, -, *150 MW*	*0.89*
Steam turbine, Siemens, -	*0.9*
Condensing turbine, AEG, *250 MW*	*0.91*
Back-pressure turbine, Leningradsky Metallichesky Zavod, *50 MW*	*0.94*

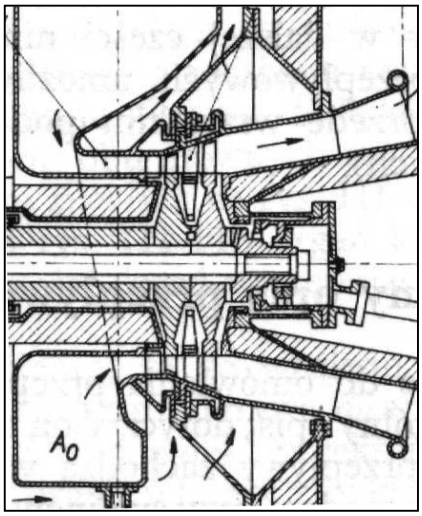

Figure 5 *– Fragment of a low-power gas turbine, 350kW, $r_h/r_t \approx 0.84$ [2].*

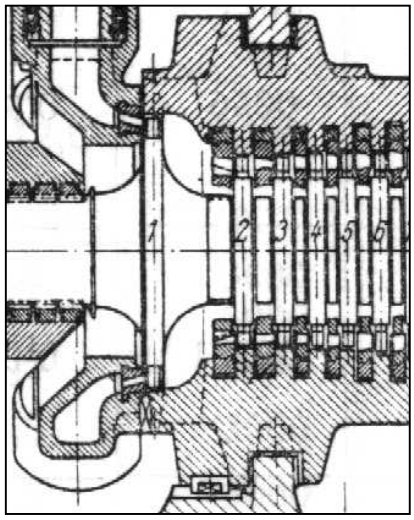

Figure 6*. - Fragment of an AEG back-pressure turbine, 5 000kW, $r_h/r_t \approx 0.88$ [2].*

Some hub-to-tip ratios were roughly calculated from the turbines' drawings provided in [2] to check their values for typical turbines. The results with a short turbines' characteristic can be found in Table 3. Figures 5 and 6 present stator rows of a gas and steam turbine, from which the hub-to-tip ratio can be approximately read. It can be seen that the hub-to-tip ratio of the first stator rows of the gas turbines can be found in the vicinity of the hub-to-tip ratio of the cascade K_D. As far as the steam turbines are concerned, their hub-to-tip ratios can be found between the hub-to-tip ratios of the cascades K_D and K_B. Cascade K_A does not seem to have any practical application. The geometries K_E and K_D are typical for test rigs, which can be seen in [8], [15], [16], [17] and [20].

The meshes were constructed by means of intersecting and subtracting volumes. The blades were stacked radially at their trailing edges. Owing to the fact that the blades are untwisted, the leading edges are offset from the radial direction. It follows that the incidence conditions, i.e. incidence angle and the incidence of the boundary layer on the leading edge, will be different for the linear cascade and each of the annular cascades. It can be expected that the differences between the flows of the cascades can be partly induced by the different incidence conditions.

The orientation of the coordinate system of the annular cascades is identical to the orientation of the coordinate system of the linear cascade. For convenience, the placement of the coordinate system was organized in such a way that the *X*-axis agrees with the axis of rotation and indicates the sense of the inflow.

The meshes of the annular cascades were produced in the following manner:

- The 2D mesh borrowed from the 2D cascade was laid onto the midspan plane of the computational domain.
- The spanwise edges were divided into the elements in the same fashion as for the linear cascade.
- The 2D mesh of the midspan plane was extruded spanwise in both directions.

For the spacing between the blades varies along the blade height of annular cascades, the cells of the mesh, especially those close to the hub and shroud, are twisted while extrusion is performed. The smaller is the value of the hub-to-tip ratio, the more distorted is the mesh. Table 4 represents characteristics of the meshes. Similarly like for the linear cascade, the "EquiAngle Skew" was employed as a measure of the mesh quality.

Table 4 *– Mesh quality of the annular cascades*

Cascade notation	K_A	K_B	K_C	K_D	K_E
Number of the elements	*180120*	*181344*	*181680*	*178344*	*196075*
"EquiAngle Skew" of the worst cell	*0.51*	*0.53*	*0.55*	*0.72*	*0.83*
Percentage of the cells in region 2 with "EquiAngle Skew" greater than 0.5	*0.02 %*	*0.03%*	*0.04%*	*0.74%*	*1.58%*
Percentage of the cells in region 2 with "EquiAngle Skew" greater than 0.75	*0*	*0*	*0*	*0*	*0.04%*

As the previously created 2D mesh was used as a pattern for extrusion of the mesh of the cascade K_E, it occurred that the resulting mesh contained cells of "EquiAngle Skew" reaching the value of *0.87*. They could deteriorate the solution or slow the convergence [5]. In order to prevent that, the 2D mesh, which was used as the pattern for the extrusion, was slightly modified, i.e. the number of the boundary layer cells around the blade was reduced from *3* to *2*. It resulted in a reduction of the skewness.

Figure 7 provides an overlook at the cascades. The geometries are exhibited in different scales. Only faces of hub and blades are shown. The mesh of the cascade K_E is depicted in Figure 8.

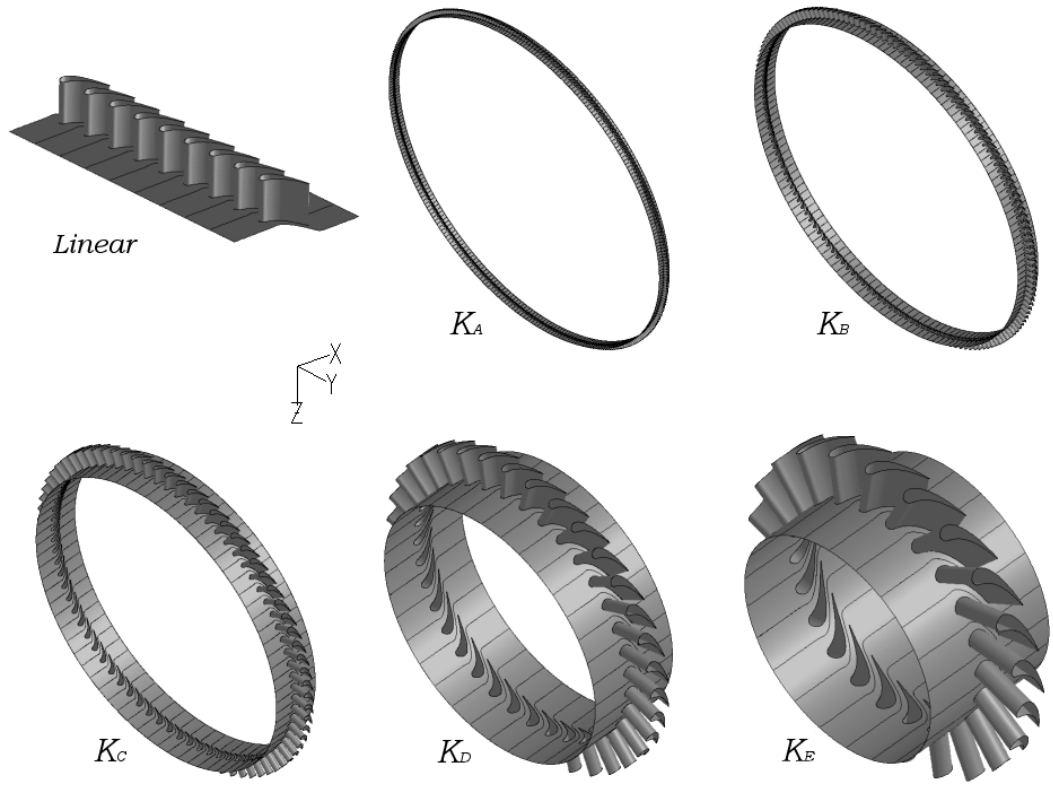

Figure 7 *– Geometries of the cascades*

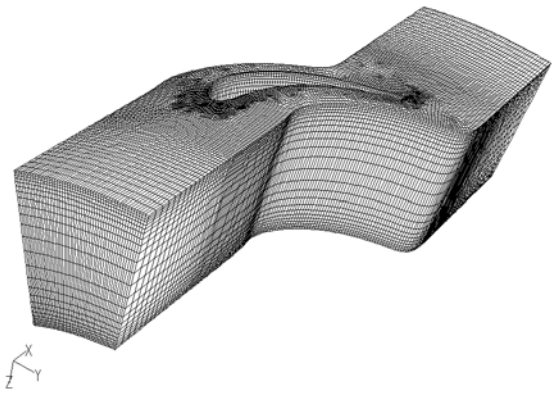

Figure 8 – *Mesh of the cascade* K_E

3 Boundary Conditions & Flowing Medium Properties

3.1 Experiment Boundary Conditions

The boundary conditions of the CFD simulation were based on the boundary conditions of the experiment described in [1]. The details about the inlet and the outlet flow as well as the characteristic of the inlet boundary layer provided by the experiment's document are shown in Table 5 and Table 6.

Table 5 *– Inlet and outlet flow data*

Inlet Mach number, M_1	*0.15*
Outlet Mach number, M_{2is}	*0.70*
Outlet Reynolds number, Re_2	*0.84 x 10^6*
Inlet angle, β_1	*76.1°*
Outlet angle, β_2	*15.8°*

Table 6 *– Inlet boundary layer data*

Inlet boundary layer displacement thickness, δ^* *[mm]*	*2.90*
Inlet boundary layer momentum thickness, δ^{**} *[mm]*	*2.18*

No details were given about the turbulence, pressure and temperature at any point. Those variables extremely influence the results of a CFD simulation. It is substantial to provide realistic values of them if it is desired to have the results of the experiment and the CFD simulation in agreement. Some effort was made to determine missing boundary conditions.

3.2 Fluid Properties

Air was chosen as the flowing medium for the simulation. It was treated as an ideal gas so that the ideal gas state equation could be used for the calculations. Since the simulation was operating in a moderate temperature range, the specific heat capacity at constant pressure could be treated as a constant. It was assigned the value of C_p*=1007 J/(kg K).* The dynamic viscosity was modelled as a piecewise linear relation because the dynamic viscosity is sensitive to temperature changes. The program was given the values of the dynamic viscosity for every ten centigrade in the operating range, so that it could find the values of the dynamic viscosity between given points by means of linear interpolation. The molecular weight of the flowing medium was assigned the value of *28.966 kg/kmol.* The data of the air properties were sourced from [22].

3.3 Outlet

3.3.1 Outlet Flow Calculation

The document [1] states that the wind tunnel where the experiment was performed is a "blow down facility", but no explicit information about the outlet pressure is provided. Owing to that fact, the outlet pressure was assumed to be equal to the atmospheric pressure p_2*=101325 Pa.* Three equations were combined together to obtain the temperature and the velocity at the outlet:

$$\mathrm{Re}_2 = \frac{c_2 \cdot c}{\nu_{T_2}}, \tag{3.1}$$

$$c_2 = M_{2is} \cdot \sqrt{\kappa \cdot R \cdot T_2}, \tag{3.2}$$

$$\nu_{T_2} = \nu_{293.15} + (T_2 - 293.15) \cdot \frac{\nu_{303.15} - \nu_{293.15}}{10}. \tag{3.3}$$

Equation (3.1) is the equation of the Reynolds number, where c_2 is the outlet velocity, c is the blade chord and ν_{T2} is the kinematic viscosity at the temperature T_2. Equation (3.2) binds the outlet velocity and the velocity of sound together. In this equation, κ is the specific heat ratio that for air equals *1.4*, $R = 287.22\ J/(kg\ K)$ is the gas constant for air and T_2 is the temperature of the outflow.

The kinematic viscosity, which is required to obtain the outlet velocity from the Reynolds number, varies significantly with temperature changes. Due to that fact, it was necessary to derive it by introducing the third equation. The values of the kinematic viscosity were given for the temperatures *293.15 K, 303.15 K*. The value of the kinematic viscosity at the outlet was obtained by linear interpolation that is expressed by Equation (3.3). ν_{T2} is the value of the kinematic viscosity corresponding to the temperature T_2.

The set of Equations (3.1), (3.2) and (3.3) was solved producing following results: $c_2 = 242.9\ m/s$, $T_2 = 299.5\ K$, $\nu_{299,5} = 15.96 \cdot 10^{-6}\ m^2/s$.

Although the above data were not required as an input of the pressure type boundary condition at the outlet, they are useful for the further inlet flow calculations. The density was calculated from the ideal gas state equation: $\rho_2 = 1.18\ kg/m^3$.

3.3.2 Outlet Pressure Profile for the Annular Cascades

As opposed to the linear cascade, an additional boundary condition feature had to be applied for the annular cascades. A simple model for the varying pressure along the blade height can be derived from the equation of the radial equilibrium condition [2]:

$$\frac{1}{\rho} \cdot \frac{\partial p}{\partial r} = \frac{c_u^2}{r}. \qquad (3.4)$$

To obtain the form of the pressure at the particular points at the outlet, it is necessary to transform the equation representing the radial equilibrium (3.4) into the integral (3.5).

$$p_2 = \int_{r_m}^{r} \rho_2 c_{u2}^2 \frac{1}{r} dr. \qquad (3.5)$$

To calculate the integral (3.5), circumferential velocity c_{u2} needs to be defined. It can be derived from the outlet velocity c_2 and the outlet flow angle β_2.

The outlet flow angle β_2 can be expressed by [3]

$$\beta_2 = \arcsin\left(\frac{o}{s}\right) + \Delta\beta_2\left(\frac{o}{s}, M_2\right). \qquad (3.6)$$

For the outlet angles β_2 =15° to 20°, the second term of Equation (3.6) is usually negligible [3] and was omitted in this case. The first term varies with the span height. It was found that in the most extreme case of the cascade K_E the term *arcsin(o/s)* would differ between values of *13.5*° and *16.5*°. Owing to the fact that it is a small variation and for the simplicity of the integration, the outlet flow angle β_2 was assumed to be constant and equal to the outlet angle of the linear cascade given in Table 5.

The velocity distribution was assumed to be uniform at the outlet. Therefore, the circumferential velocity c_{u2} became a constant and was calculated from β_2 and c_2 producing the value of *234 m/s*. Should the density at the outlet be assumed constant as well, the pressure at the distance r from the axis of rotation can be represented by

$$p_2 = \rho_2 \cdot c_{u2}^2 \cdot \ln\frac{r}{r_m} + p_{2m}. \qquad (3.7)$$

The pressure at the radius r_m was given the value *101325 Pa* due to the fact that the pressure at the distance $r = r_m$ was assumed to be equal to the outlet pressure of the linear cascade. The pressure profile was implemented into FLUENT by means of a UDF presented in Appendix A.

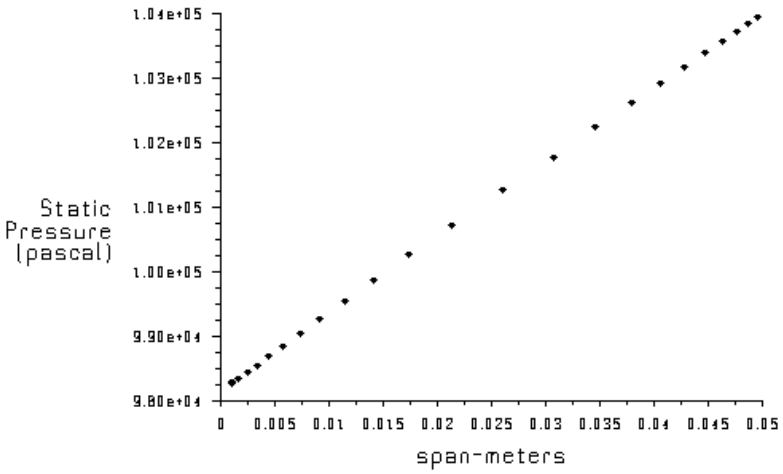

Figure 9 *– Exemplary outlet pressure distribution of the cascade* K_B.

Since the factor r/r_m of the annular cascades that were considered in this thesis oscillates close the value of *1*, the outlet pressure profile resembles a straight line. It can be seen in Figure 9. For the outlet of cascades having lower hub-to-tip ratio, the outlet pressure will obtain the form of the logarithmic function.

It should be underlined that the pressure profile is relatively simple. It is difficult to provide a realistic and detailed pressure distribution for the radial equilibrium condition. The circumferential velocity is influenced by the boundary layer, turning the passage, secondary flows etc. Therefore, it is tough to derive a realistic pressure distribution analytically.

3.3.3 Backflow Turbulence Specification

No backflow is expected for the final solution when the radial equilibrium condition is applied at the outlet. However, it appears very often during the run of the iterations when the flow in the annular cascades is calculated. It is a good custom to give realistic values of the backflow turbulence because it can help convergence and can lead to a faster solution [4].

To show the effects of the pressure distribution derived from the radial equilibrium condition, the flow through the annular cascades with the uniform pressure distribution at the outlet were simulated. In these cases, a backflow appeared for the final solutions of certain cascades and the backflow turbulence required to be specified.

Turbulence intensity I and turbulence length scale λ were chosen as the method of the turbulence specification. The former was obtained using the equation given in [4]:

$$I_2 = \frac{RMS(c^l)}{c_{avg}} = 0.16 \cdot (\mathrm{Re}_2)^{-\frac{1}{8}}. \qquad (3.8)$$

The latter can be derived from [4]

$$\lambda_2 = 0.07 \cdot D_H = 0.07 \cdot \frac{4A_o}{S_o}. \qquad (3.9)$$

Where D_H is the hydraulic diameter denoted as the ratio of the quadruple area of the blade opening A_o to the circumference of the opening S_o.

The turbulence length scale λ_2 obtained from Equation (3.9) appears to be in accordance with the real values. It was checked that the mass averaged turbulence length scale at the outflow of linear cascade equals approximately λ_2*=0.0013 m*. It was born in mind that the turbulence of the backflow formed usually by the vortex caused by the separation of the boundary layer can have different characteristics. However, due to the difficulties in deriving realistic values, Equations (3.8) and (3.9) were used to get the turbulence specification. The results are: I_2 *= 2.9%,* λ_2 *= 0.0012m*.

3.4 Inlet

3.4.1 Inlet Mass Flow Calculation

Although it would have been more straightforward to apply the velocity inlet boundary condition to model the inlet boundary layer, the inlet mass flux boundary condition was employed. The decision was based on the fact that the velocity boundary condition is disapproved when calculating compressible flows [4].

Should the total enthalpy of the flow through the cascade be assumed constant, the temperature at the inlet T_1 can be expressed by

$$T_1 = \frac{C_p T_2 + \frac{1}{2} c_2^2}{C_p + \frac{1}{2} M_1^2 \kappa \cdot R}. \qquad (3.10)$$

The inlet velocity c_1 was substituted for

$$c_1 = M_1 \sqrt{\kappa R T_1}. \qquad (3.11)$$

If it is assumed that the flow is steady and the density is constant at both inlet and outlet, it can be stated from the mass conservation rule:

$$\rho_1 = \rho_2 \frac{c_{2x}}{c_{1x}}. \qquad (3.12)$$

The mass flux Φ_1 is defined as

$$\Phi_1 = \rho_1 c_{1x}. \qquad (3.13)$$

The inlet velocity in the X-direction was calculated from the inlet velocity and the inlet flow angle. The set of Equations (3.10) till (3.13) gave following results: $T_1 = 327.3\ K$, $c_1 = 54.4\ m/s$, $\rho_1 = 1.48\ kg/m^3$, $\Phi_1 = 78.2\ kg/(s\ m^2)$.

A mass flow boundary condition requires, besides the value of the mass flux, the direction of the flow. For the linear cascade, the flow direction is given by:

$$cmp_{1x} = \sin \beta_1, \tag{3.14}$$

$$cmp_{1y} = \cos \beta_1, \tag{3.15}$$

$$cmp_{1z} = 0. \tag{3.16}$$

For an annular cascade, the direction of the inlet flow and its components of the *Y*- and *Z*-velocities in an orthogonal coordinate system vary for different points at the inlet. Therefore, it was necessary to introduce additional equations defining the inlet flow direction for the annular cascades. The flow direction at the outlet of the annular cascades that have the origin of their coordinate system in the center of rotation can be described by:

$$cmp_{1x}^{ann} = \sin \beta_1, \tag{3.17}$$

$$cmp_{1y}^{ann} = \cos \beta_1 \frac{z}{\sqrt{y^2 + z^2}}, \tag{3.18}$$

$$cmp_{1z}^{ann} = \cos \beta_1 \frac{y}{\sqrt{y^2 + z^2}}. \tag{3.19}$$

To obtain the values of the inlet velocity in particular directions it is required to multiply Equations (3.17) to (3.19) by c_1. Whereas the *Y*- and *Z*-components vary for different spots of the inlet, the *X*-component remains constant. It was necessary to employ a UDF to define the inlet velocity components of the annular cascades. Examples are given in Appendix A.

3.4.2 Inlet Boundary Layer

The form of the inlet boundary layer influences the behaviour of the secondary flows at the spot where it encounters the blade and when the flow moves farther downstream [2]. The details about the experiment's boundary layer are provided within Table 6.

The inlet boundary layer displacement thickness $\delta*$ and the inlet boundary layer momentum thickness $\delta**$ are respectively given by [6]:

$$\delta* = \int_0^{\delta} \left(1 - \frac{c}{c_\infty}\right) dz, \qquad (3.20)$$

$$\delta** = \int_0^{\delta} \frac{c}{c_\infty} \left(1 - \frac{c}{c_\infty}\right) dz. \qquad (3.21)$$

The notation δ is the height of the boundary layer defined to be a distance from the wall where the difference between the velocity of the flow c_δ and the undisturbed velocity of the main flow c_∞ far away from the wall is smaller or equal to *1%*.

The velocity magnitude in a boundary layer at distance z from the wall is usually described by an one-term polynomial function of the fractional exponent:

$$c = c_\infty \left(\frac{z}{\delta}\right)^{\frac{1}{k}}. \qquad (3.22)$$

To fix the values of k and δ, the velocities in Equations (3.20) and (3.21) need to be substituted for Equation (3.22). If those two equations are integrated afterwards, following set of equations is produced:

$$k = \frac{2\delta**}{\delta* - \delta**}, \qquad (3.23)$$

$$\delta = \delta*(1 + k). \qquad (3.24)$$

It can be calculated from the data in Table 6 that: $k = 6$, $\delta = 0.02\ m$. For it was decided to use the mass flux as the boundary condition at the outlet, Equations (3.13) and (3.22) were combined together to obtain the form of the mass flux at the inlet. The shape of the inlet velocity profile is presented in Figure 10. It can be seen that it has a relatively large boundary layer thickness.

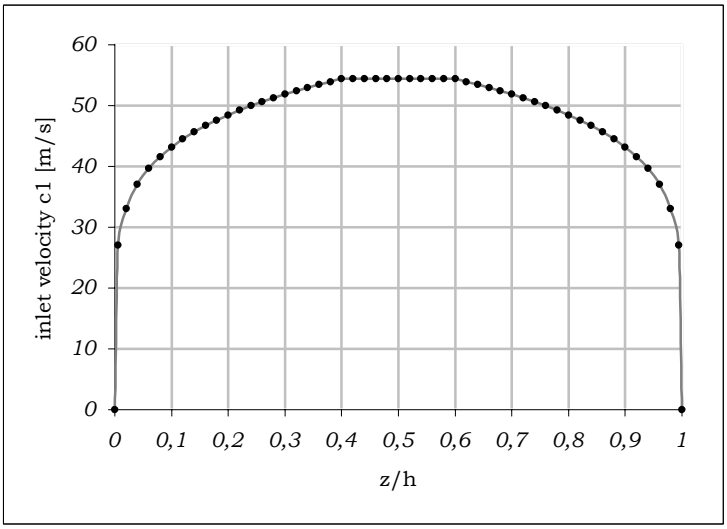

Figure 10 – *Velocity profile at the inlet.*

The form of the velocity profile at the inlet was modelled in FLUENT by means of a UDF. An example for it is given in Appendix A.

3.4.3 Inlet Turbulence Specification

Turbulence intensity and turbulence length scale were chosen as the method of the turbulence specification. Since no explicit information was given for the turbulence, its characteristics needed to be based on a judgement. For this purpose, a couple of simulations had been done to adjust its values. Finally, it was decided that the inlet turbulence length scale λ_1 would equal one percent of the span height, whereas the turbulence intensity I_1 would be given the same value as at the outlet: $I_1 = 2.9\%$, $\lambda_1 = 0.01 \cdot h = 0.00055\ m$.

3.5 Walls

Two significant features were applied for the walls' boundary conditions:

- Since the process was assumed to be adiabatic, the value of heat flux through the walls was set to be equal zero.
- No slip condition was applied at the walls.

3.6 Periodicity

Since the computational domain consists of repetitive sections, a periodic boundary condition was utilized to reduce the computational effort. Mesh surfaces where the boundary condition was used were coupled in GAMBIT so that every node on one wall had a corresponding node on the corresponding surface.

4 Solution Methods

4.1 Solver

FLUENT is a program working on the basis of the finite volume method; the domain is divided into control volumes and the integral form of the equations of conservation of mass, momentum and energy is solved after the discretization.

Between two types of the solvers offered by FLUENT, the segregated solver was used. In this solver, equations of continuity, momentum and, at the end, energy and turbulence are solved in sequence. Consequently, the convergence is checked. If the residuals do not reach a given level, the properties of the flow are updated and the solution of the equations is repeated [4]. The flow was simulated as steady.

In computational methods, the governing equations need to be translated into a form understandable by the computer, which is done by means of the discretization. It was chosen to use first-order upwind discretization for the initial part of the solution to help the convergence. Eventually, it was set to second-order upwind to obtain more accurate results.

The governing equations are linearized by a so called implicit linearization. For every cell there exists one equation of each flow variable (pressure, *X*-momentum etc.) consisting of the existing and unknown variables from the neighbouring cells [4]. This set of equations is solved with the help of the methods presented in [4].

4.2 Turbulence Modelling

A flow having high Reynolds numbers usually involves turbulence length scales that are much smaller than the size of the control volumes. Therefore, it is common to employ statistical models to simulate the turbulence. The standard k-ε turbulence model offered in FLUENT was used for the purpose of these simulations. This semi-empirical model is adequate for fully turbulent flows. This model is based on the transport equations of the turbulence kinetic energy k and on the turbulence dissipation rate ε [4]. The effects of the molecular viscosity are assumed to be negligible. The standard model constants ($C_{1\varepsilon}$, $C_{2\varepsilon}$ etc.) suggested in [4] were employed.

4.3 Wall Function

Walls affect greatly the behaviour of the flow. In the vicinity of the walls the velocity fluctuations are damped and viscous effects become more important [4]. Since the viscous forces are omitted in the k-ε model, the viscosity affected flow in the region very close to the walls is not resolved by the equations that are used in general for the flow simulation. Instead, special functions are used to model the behaviour of the flow that is close to the walls. In this simulation, the standard wall function offered in FLUENT was used.

The document [4] suggests that the dimensionless wall distance y^+ is kept as close as possible to *30* but no smaller than this value to model properly the flow in the vicinity of the walls. It was checked that the value of y^+ oscillates between *17* and *235* for the final solution of the 3D cascades. The regions having y^+ smaller than *30* existing in the area of the stagnation of the flow (leading edge) were relatively small however.

5 Criteria & Methods of the Flow Investigation

5.1 Isentropic Mach Number

The isentropic Mach number M_{is} at a point can be defined as the ratio of the velocity that would be produced from isentropic expansion from total to static conditions at this point to the velocity of sound in the total conditions at this point:

$$M_{is} = \frac{c_s}{a_t} = \frac{\sqrt{2 \cdot Cp \cdot T_t \left(\left(\frac{p_t}{p} \right)^{\frac{\kappa-1}{\kappa}} - 1 \right)}}{\sqrt{\kappa \cdot R \cdot T_t}}. \qquad (5.1)$$

Equation (5.1) can be presented after some rearrangements in a simpler form:

$$M_{is} = \sqrt{\frac{2}{\kappa - 1}\left(\left(\frac{p_t}{p}\right)^{\frac{\kappa-1}{\kappa}} - 1\right)}. \qquad (5.2)$$

The isentropic Mach number is a function of the static pressure. It can be used as a tool for the flow investigation around a turbine blade. Stagnation points, fluid acceleration and deceleration at particular spots of a blade as well as the blade loading can be found using this method.

5.2 Measuring Plane

Several flow characteristics were examined on the measuring plane. The measuring plane was moved away from the leading edge with the distance of one and a half of the axial chord and oriented in such a way that it was parallel to the *YZ*-plane of the coordinate system. "The measurement plane was selected far enough from the trailing edge, where most of the energy dissipation has already taken place and the loss coefficient is representative of the overall energy dissipation" [1]. The results on the measuring plane are presented in such a manner that the direction of looking is opposite to the direction of the *X*-axis.

5.3 Outlet Flow Angle

The flow angle is one of the features that characterise the flow in a blade row. Cylindrical blades in the annular arrangement are expected to have a particular influence on the outlet flow angle.

The outlet flow angle β_2 at a certain point having coordinates (y,z) on the measuring plane is defined by

$$\beta_{2(y,z)} = \arctan \frac{c_{2x(y,z)}}{\sqrt{c_{2y(y,z)}^2 + c_{2z(y,z)}^2}}. \qquad (5.3)$$

The outlet flow angles will be investigated by means of the mass averaged outlet flow angle over the whole outlet and by means of the area averaged outlet angle at the midspan. Additionally, the pitchwise averaged deviation from the midspan outlet flow angle $\Delta\beta_2$ will be presented, which is defined by

$$\Delta\beta_{2(z)} = \overline{\beta}_{2MS} - \overline{\beta}_{2(z)}. \qquad (5.4)$$

5.4 LKEL

The LKEL at a point *(y,z)* on the plane perpendicular to the *X*-axis downstream of the cascade was defined as the difference between the squared isentropic velocity at this point and its corresponding squared real value divided by the squared pitchwise averaged value of the isentropic velocity at the midspan:

$$LKEL = \frac{c_{2s(y,z)}^2 - c_{2(y,z)}^2}{\bar{c}_{2sMS}^2} \qquad (5.5)$$

Equation (5.5) consists of some components expressing isentropic values that have to be calculated analytically to obtain the value of LKEL. Hence, it will hamper the implementation of this equation when performing the postprocessing of the solution if the equation stays in such a form.

Figure 11 represents a graph of the adiabatic expansion in a stator row. It can be noticed that in this case, the specific kinetic energy $c_2^2/2$ is the enthalpy difference during the isentropic expansion as if the isentropic expansion was performed from the total pressure p_{t2} to the static pressure p_2. The isentropic specific kinetic energy $c_{2s}^2/2$ is the enthalpy difference during the expansion as if the isentropic expansion was carried out from the total pressure p_{t1} to the static pressure p_2. If the above is taken in account, Equation (5.6) can be formulated.

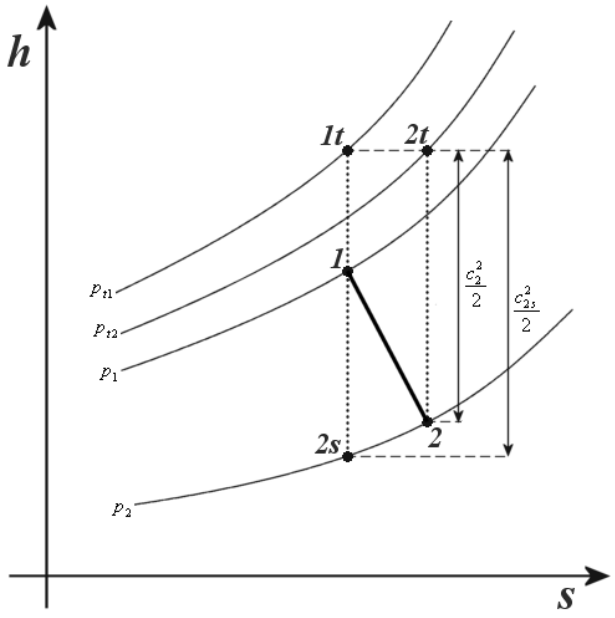

Figure 11 *– h-s diagram of the adiabatic expansion in a stator row.*

$$LKEL = \frac{Cp \cdot T_{t1}\left(\left(\frac{p_{2(y,z)}}{p_{t1(y,z)}}\right)^{\frac{\kappa-1}{\kappa}} - 1\right) - Cp \cdot T_{t2}\left(\left(\frac{p_{2(y,z)}}{p_{t2(y,z)}}\right)^{\frac{\kappa-1}{\kappa}} - 1\right)}{Cp \cdot T_{t1MS}\left(\left(\frac{\overline{p}_{2MS}}{\overline{p}_{t1MS}}\right)^{\frac{\kappa-1}{\kappa}} - 1\right)} \quad (5.6)$$

The expansion in the stator row is assumed to be adiabatic. Hence, the total enthalpy is constant. Due to the narrow range of operating temperatures, the specific heat capacity at a constant pressure can be assumed constant as well. Moreover, the total enthalpy for an inlet boundary layer does not vary usually within span height. By the reason of the above facts, the terms representing total enthalpies can be cancelled both in nominator and denominator of the Equation (5.6) forming

$$LKEL = \frac{\left(\frac{p_{2(y,z)}}{p_{t1(y,z)}}\right)^{\frac{\kappa-1}{\kappa}} - \left(\frac{p_{2(y,z)}}{p_{t2(y,z)}}\right)^{\frac{\kappa-1}{\kappa}}}{\left(\frac{\overline{p}_{2MS}}{\overline{p}_{t1MS}}\right)^{\frac{\kappa-1}{\kappa}} - 1}. \quad (5.7)$$

It is sufficient to know the total pressures at the outlet and inlet and the static pressure at the outlet to find the value of the LKEL by means of Equation (5.7). In order to apply Equation (5.7) for the postprocessing, it was required to introduce it by means of a UDF. The program with a short description can be found in Appendix A.

5.5 Vorticity

Vorticity is a vector field defined as curl of the velocity vector field. It is represented by [10]

$$\vec{\xi} = \nabla \times \vec{c}. \tag{5.8}$$

The components of the vorticity in a Cartesian coordinate system are defined by [6]:

$$\xi_x = \frac{\partial c_z}{\partial y} - \frac{\partial c_y}{\partial z}, \tag{5.9}$$

$$\xi_y = \frac{\partial c_x}{\partial z} - \frac{\partial c_z}{\partial x}, \tag{5.10}$$

$$\xi_z = \frac{\partial c_y}{\partial x} - \frac{\partial c_x}{\partial y}. \tag{5.11}$$

The streamwise vorticity was used for the postprocessing of the results. It can be obtained as a projection of the local vorticity vector on the direction of the primary outlet flow. In this case, every vorticity component was projected onto this direction and then added.

The streamwise vorticity for the linear cascade is given by

$$\xi_{stream} = \xi_x \sin\overline{\beta}_{2MS} + \xi_y \cos\overline{\beta}_{2MS}, \tag{5.12}$$

while for the annular cascades it is expressed by

$$\xi_{stream}^{ann} = \xi_x \sin\overline{\beta}_{2MS} + (\xi_y \cos\theta + \xi_z \sin\theta)\cos\overline{\beta}_{2MS}. \tag{5.13}$$

The angle θ can be found from the geometrical relation exhibited in Figure 16 (Equation (5.29)).

5.6 Secondary Velocity Vectors

The secondary velocity vector $\vec{c}_{\sec}$ is defined as the difference between the local velocity vector $\vec{c}$ and the primary velocity vector $\vec{c}_{prim}$:

$$\vec{c}_{\sec} = \vec{c} - \vec{c}_{prim}. \qquad (5.14)$$

In general, the secondary velocity vectors are very sensitive to the formulation of the primary velocity vector. In this work, secondary velocity vectors were defined as the projection of the local velocity vector onto the plane perpendicular to the primary flow. The projected secondary velocity vectors $\vec{c}_{proj}$ were visualised on the measuring plane. Since the measuring plane lies perpendicularly to the *X*-axis, there will be *Y*- and *Z*-components of the secondary velocities.

5.6.1 Secondary Velocity Vectors for the Linear Cascade

As far as the linear cascade is concerned, it can be observed from Figure 12 and Figure 13 that the vectors defined as a projection of the local velocity vector onto the plane perpendicular to the primary flow can be expressed by

$$\begin{bmatrix} \vec{c}_{proj,y} \\ \vec{c}_{proj,z} \end{bmatrix} = \begin{bmatrix} -\left|\vec{c}_{XY}\right| \sin(\beta_{XY} - \beta_{prim,XY}) \\ \left|\vec{c}_{YZ}\right| \sin(\beta_{YZ} - \beta_{prim,YZ}) \end{bmatrix}. \qquad (5.15)$$

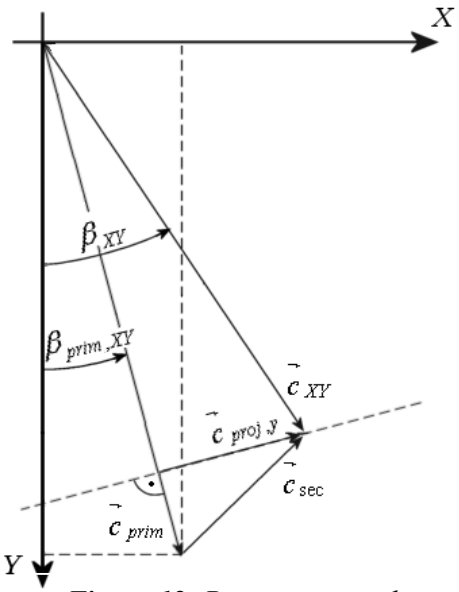

***Figure 12**- Primary, secondary and local velocity vectors for the linear cascade on the XY-plane.*

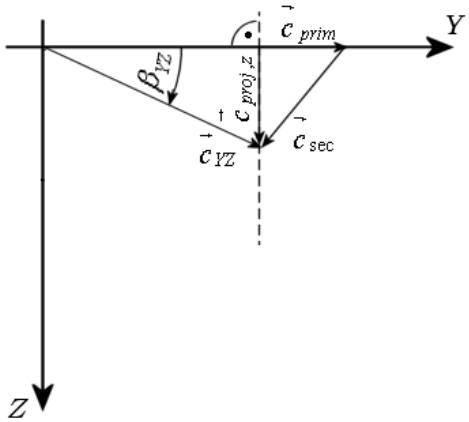

***Figure 13**- Primary, secondary and local velocity vectors for the linear cascade on the YZ-plane.*

Since it was chosen that the area averaged midspan velocity vector would represent the primary velocity vector, the primary outlet flow angle on the *XY*-plane can be assigned the value of the area averaged outlet flow angle at midspan:

$$\beta_{prim,XY} = \overline{\beta}_{2MS}. \tag{5.16}$$

The primary velocity vector lies on the *XY*-plane. Therefore,

$$\beta_{prim,YZ} = 0. \tag{5.17}$$

The outlet flow angle of the local velocity on the *XY*-plane can be represented as

$$\beta_{XY} = \arctan\frac{c_x}{c_y}. \tag{5.18}$$

Finally, the components of the projected local velocity vector onto the plane perpendicular to the primary flow can be expressed by

$$\begin{bmatrix} \vec{c}_{proj,y} \\ \vec{c}_{proj,z} \end{bmatrix} = \begin{bmatrix} \sqrt{c_x^2 + c_y^2}\,\sin(\overline{\beta}_{2MS} - \arctan\frac{c_x}{c_y}) \\ c_z \end{bmatrix}. \tag{5.19}$$

5.6.2 Secondary Velocity Vectors for the Annular Cascades

It can be seen in Figure 14 and Figure 15 that the projected secondary velocity vector for the annular cascades can be obtained similarly as for the linear cascade:

$$\begin{bmatrix} \vec{c}^{\,ann}_{proj,y} \\ \vec{c}^{\,ann}_{proj,z} \end{bmatrix} = \begin{bmatrix} -\left|\vec{c}_{XY}\right|\sin(\beta_{XY} - \beta_{prim,XY}) \\ \left|\vec{c}_{YZ}\right|\sin(\beta_{YZ} - \beta_{prim,YZ}) \end{bmatrix}. \tag{5.20}$$

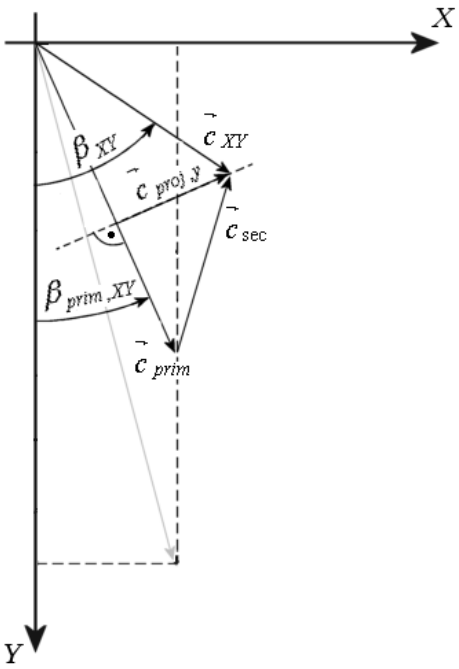

***Figure 14**- Primary, secondary and local velocity vectors for the annular cascades on the XY-plane*

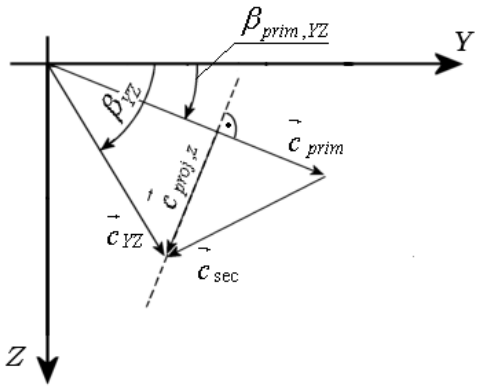

***Figure 15**- Primary, secondary and local velocity vectors for the annular cascades on the XY-plane*

The outlet angles on the *XY*-plane and on the *YZ*-plane can be respectively described as:

$$\beta_{XY} = \arctan\frac{c_x}{c_y}, \tag{5.21}$$

$$\beta_{YZ} = \arctan\frac{c_z}{c_y}. \tag{5.22}$$

For the annular cascades, the outlet angle $\beta_{prim,XY}$ varies on the *XY*-plane and cannot be assigned the constant value of the area averaged midspan velocity. It can be seen in Figure 14 that for the annular cascades

$$\tan\beta_{prim,XY} = \frac{c_{prim,x}}{c_{prim,y}}. \tag{5.23}$$

Similarly as for the linear cascade, the primary vector of the annular cascades is represented by the area averaged outlet flow at midspan.

The area averaged outlet flow angle at midspan can be defined as:

$$\tan \overline{\beta}_{2MS} = \frac{c_{2MS,x}}{c_{2MS,u}} = \frac{c_{prim,x}}{c_{prim,u}}. \qquad (5.24)$$

It can be seen in Figure 16 that the primary circumferential velocity $c_{prim,u}$ can be related with the primary Y-velocity for the annular cascades $c_{prim,y}$ in the following way:

$$\frac{c_{prim,y}}{c_{prim,u}} = \cos\theta = \frac{|z|}{\sqrt{y^2 + z^2}}. \qquad (5.25)$$

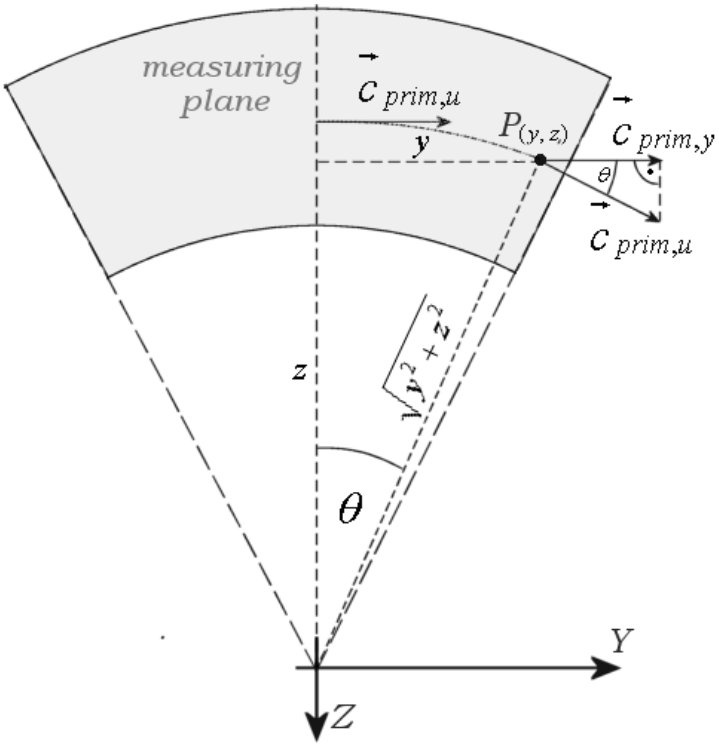

***Figure 16** – Primary velocity vector for annular cascades on the measuring plane.*

If Equations (5.23), (5.24) and (5.25) are combined together the following can be obtained:

$$\tan \beta_{prim,XY} = \frac{\sqrt{y^2 + z^2}\, \tan \overline{\beta}_{2MS}}{|z|}. \qquad (5.27)$$

The outlet angle $\beta_{prim,XY}$ can be expressed as the inverse of the function in Equation (5.27):

$$\beta_{prim,XY} = \arctan \frac{\sqrt{y^2 + z^2}\, \tan \overline{\beta}_{2MS}}{|z|}. \tag{5.28}$$

It can be seen from Figure 16 that

$$\beta_{prim,YZ} = \theta = \arctan \frac{y}{|z|}. \tag{5.29}$$

Eventually, the components of the projected secondary velocity vector for the annular cascades can be defined as:

$$\begin{bmatrix} \vec{c}_{proj,y}^{\,ann} \\ \vec{c}_{proj,z}^{\,ann} \end{bmatrix} = \begin{bmatrix} \sqrt{c_x^2 + c_y^2} \sin\left(\arctan \frac{\sqrt{y^2 + z^2}\, \tan \overline{\beta}_{2MS}}{|z|} - \arctan \frac{c_x}{c_y} \right) \\ \sqrt{c_y^2 + c_z^2} \sin\left(\arctan \frac{c_z}{c_y} - \arctan \frac{y}{|z|} \right) \end{bmatrix}. \tag{5.30}$$

It can be noticed in Figures 14 and 15 that the vector $\vec{c}_{proj,y}$ mirrors *X*- and *Y*-components whereas the vector $\vec{c}_{proj,z}$ mirrors *Y*- and *Z*-components of the secondary velocities. Equations (5.19) and (5.30) were introduced into FLUENT by means of the custom field functions. The area averaged outlet flow angle at midspan was averaged separately for each cascade.

5.7 Definition of Losses

There are a few loss definitions in use. Two of the most typical are: the total pressure loss coefficient Y and the enthalpy loss coefficient ζ [9]:

$$Y = \frac{p_{t1} - p_{t2}}{p_{t2} - p_2}, \tag{5.31}$$

$$\zeta = \frac{h_2 - h_{2s}}{h_{t2} - h_2}. \tag{5.32}$$

Equation (5.32) can be transformed into

$$\zeta = \frac{c_{2s}^2 - c_2^2}{c_2^2}. \tag{5.33}$$

It can be seen that Equation (5.33) is very similar to Equation (5.5), which is used for the LKEL plots. The only difference is the denominator. LKEL is expected to be slightly smaller in comparison to the enthalpy loss coefficient because the midspan isentropic velocity c_{2sMS} is usually larger than the local velocity c_2.

It was chosen that the total loss would be represented by the mass average of LKEL. Midspan loss, which is often denoted as the profile loss, was expressed as the area average LKEL at midspan of the linear cascade. The secondary losses for each hub-to-tip ratio were obtained by subtraction of the midspan loss of the linear cascade from the total loss of the cascade.

6 CFD Results & Discussion

6.1 Uniform Outlet Pressure Distribution vs. Radial Equilibrium Condition

The uniform pressure distribution was applied at the outlet for the initial simulations. Whereas there were no extraordinary phenomena in the case of the cascade K_A, backflow appeared at the outlet for the cascades K_C, K_D and K_E. It resulted from the eddy caused by the boundary layer separation at the hub. As far as the cascade K_B is concerned, there were residuals' oscillations at the very low level for the final solution.

It was caused by the flow that was on the verge of separation for the cascade K_B, i.e. there was backflow or very little backflow for successive final iterations. The results of the CFD simulation correspond to the calculations worked out in [11].

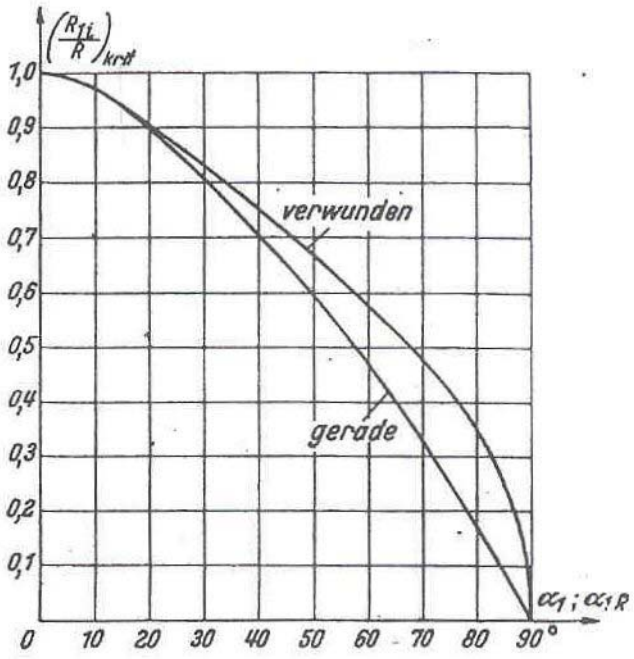

***Figure 17** – Critical hub-to-tip ratio in relation to the outlet angle [11]*

Figure 17 exhibits the dependence of the outlet flow angle on the critical hub-to-tip ratio, i.e. the value of the hub-to-tip ratio for which the separation develops if the pressure at the outlet is uniform. The line denoted as "*gerade*" corresponds to the cylindrical blades, which are of interest here. It can be seen that for the values of $\beta_2 \cong 15°$ (α_1 in the figure), the value of the critical hub-to-tip ratio is approximately *0.95*, which corresponds to the hub-to-tip ratio of the cascade K_B. The larger is the outlet flow angle, the larger is the range of the hub-to-tip ratios without flow separation. For example, for a cascade having the outlet flow angle of *30*° and hub-to-tip ratio equal *0.9*, i.e. for a typical stator row geometry from an HP turbine, there is no separation expected.

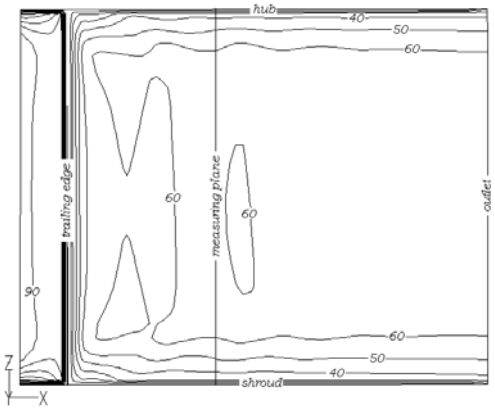

Figure 18 *- Axial velocity contours on the plane at y=0 downstream of the cascade K_A with the radial equilibrium condition.*

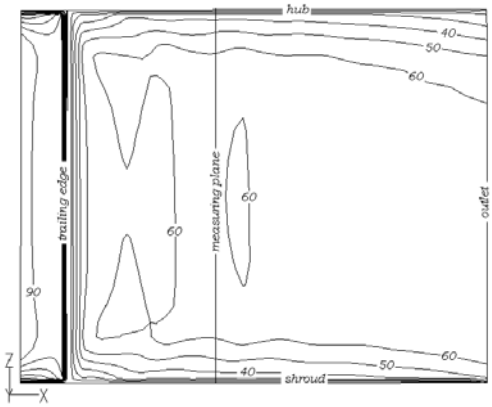

Figure 19 *- Axial velocity contours on the plane at y=0 downstream of the cascade K_A without the radial equilibrium condition*

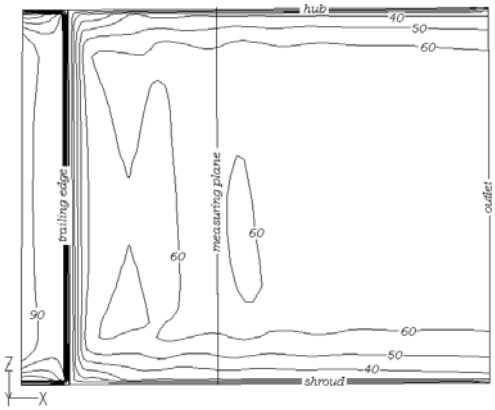

Figure 20*- Axial velocity contours on the plane at y=0 downstream of the cascade K_B with the radial equilibrium condition.*

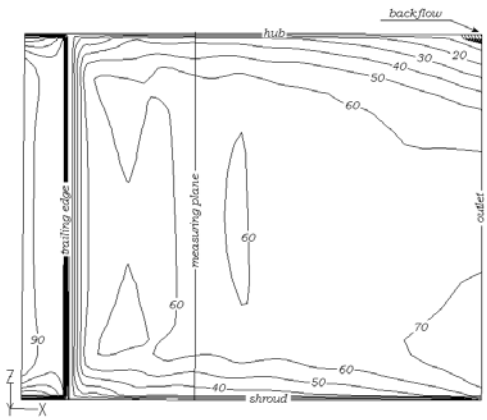

Figure 21 *- Axial velocity contours on the plane at y=0 downstream of the cascade K_B without the radial equilibrium condition.*

If the radial equilibrium condition is employed at the outlet, flow separation does not occur for any of the investigated hub-to-tip ratios. It is evident that the boundary layer separation changes dramatically the flow downstream of the cascade. The question arises what would be the differences between the flow with and without radial equilibrium when separation does not appear for both boundary condition types. To investigate this, a plane at constant *y=0* was constructed downstream of the cascade. Figures 18 and 19 show the comparison of the axial velocity for the cascade K_A with two different boundary conditions at the outlet. A velocity drop due to the excessive pressure value is visible near the hub of the cascade K_A when uniform pressure distribution is applied. The same feature is

compared in Figure 20 and Figure 21 for the cascade K_B. A visible decrease in the axial velocity can be noticed near the hub if uniform pressure distribution is applied for this cascade. A small backflow appears in the vicinity of the hub wall near the outlet.

Figure 22 depicts exemplary behaviour of the flow when uniform pressure distribution is applied at the outlet and a backflow appears at the outlet.

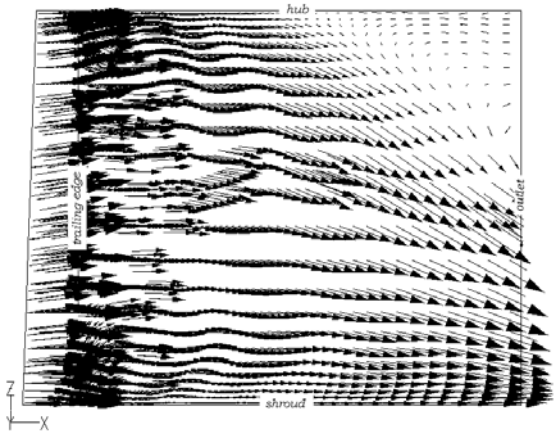

Figure 22 *- Velocity vectors on the plane y=0 downstream of the cascade K_D without the radial equilibrium condition.*

On the one hand, the flow in the investigation area, i.e. on the measuring plane, and the flow upstream do not seem to be remarkably influenced by the uniformity of the pressure distribution. On the other hand, it is obvious that it is substantial to provide realistic boundary conditions if it is deserved to simulate the reality in detail. The further CFD results are presented only for the simulations when radial equilibrium condition was applied at the outlet.

6.2 Isentropic Mach Number Distribution around the Blade

Equation (5.2) was employed to obtain the isentropic Mach number distribution around the blade at the midspan. The total pressure p_t in this equation was calculated as the area average total pressure at the midspan of the inlet. Figure 23 represents the comparison of the experiment [1] and CFD results of the isentropic Mach number distribution for the linear cascade. It can be noticed that there are significant differences on the suction side, whereas the pressure side results stays relatively well in agreement. In the experiment, the flow is much higher accelerated just at the leading edge and has a considerably higher value of the isentropic Mach number throughout nearly the whole length of the blade in comparison to the CFD experiment. What follows, the blade loading, which is proportional to the isentropic Mach number difference between suction and pressure side, proves to be much higher in the real experiment. The maximum velocity spots corresponding to the maximum isentropic Mach number diverge also for both cases; the maximum velocity point is shifted father downstream in case of the CFD solution. In both cases, the velocity at the pressure side remains at low level for the first half of the blade followed by the gradual velocity increase for the second half.

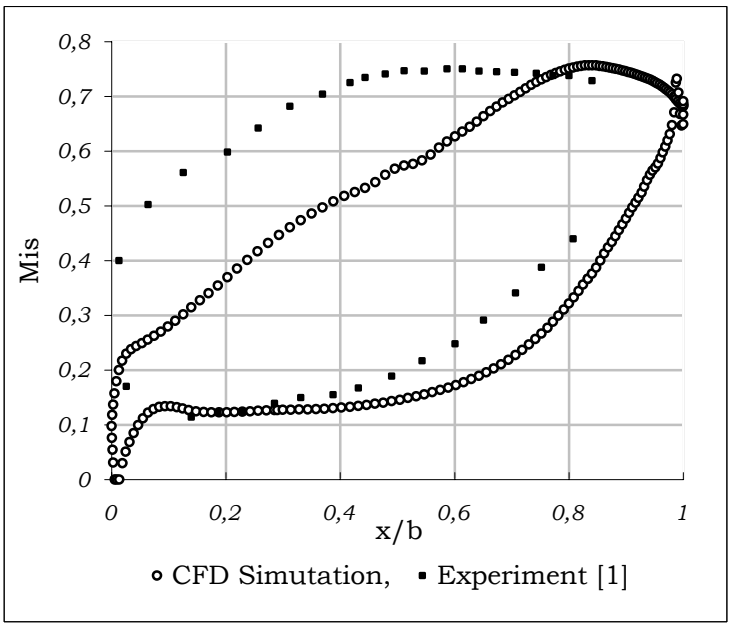

***Figure 23** - Isentropic Mach number distribution around the blade at midspan. Comparison of the CFD and experiment results [1].*

There could be several reasons for the relatively big differences between the results of both methods. It is likely that the boundary conditions of the experiment and CFD simulation did not correspond with each other. Mainly, the boundary conditions that were not specified explicitly in the experiment document, i.e. the outlet pressure and the turbulence specification. Moreover, both methods, but mainly computational method, for which simplifications were done, are bound to introduce errors.

It was found that the hub-to-tip ratio does not have a significant influence on the isentropic Mach number distribution at the midspan of the blade. It means that the behaviour of the flow at the midspan is expected to be very similar for all the cascades. Figure 24 exhibits the comparison of the isentropic Mach number distribution at midspan for two extreme hub-to-tip ratios, i.e. for the linear cascade and for cascade K_E.

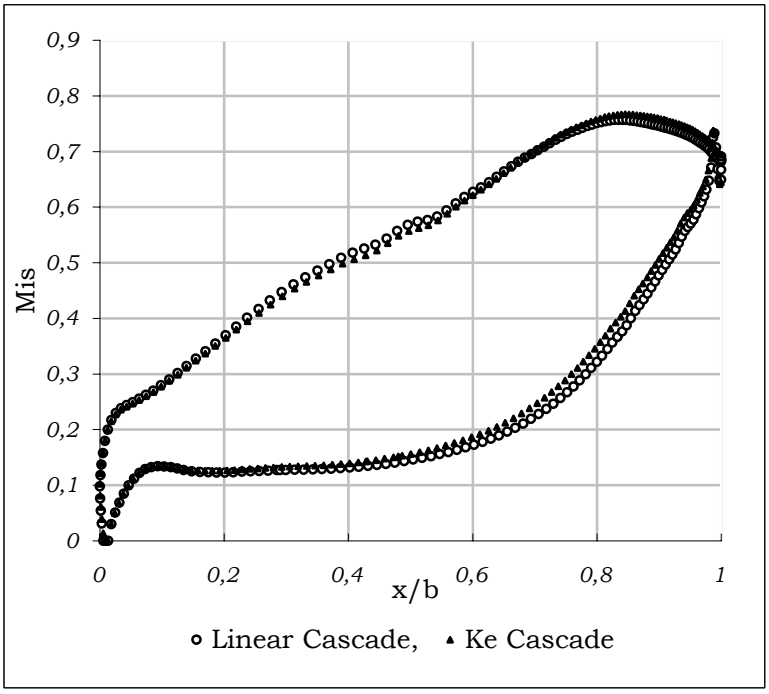

Figure 24– *Isentropic Mach number distribution around the blade at the midspan for the linear cascade and the cascade* K_E.

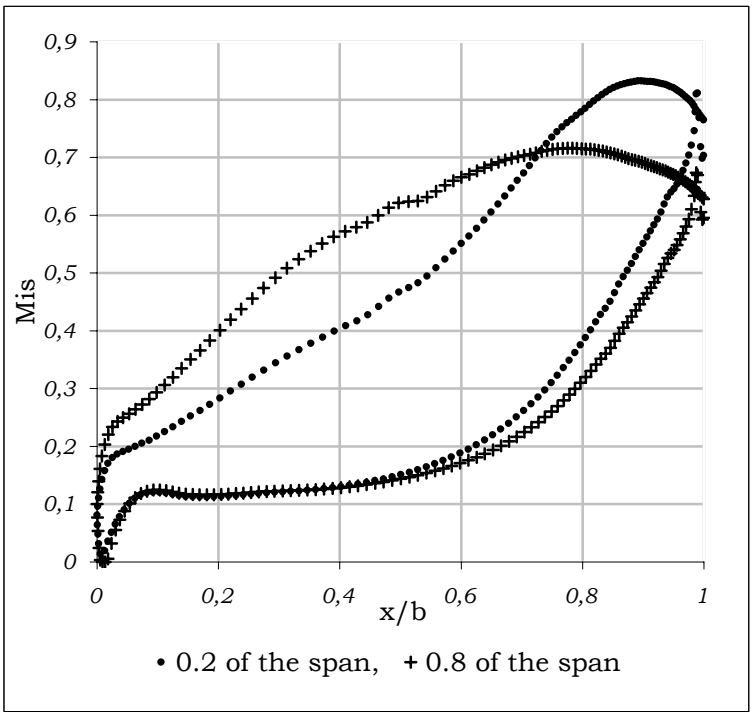

***Figure 25**- Isentropic Mach number distribution around the blade at 0.2 and 0.8 of the span for the cascade K_E*

Although the behaviour of the flow at midspan for all cascades proves to be very similar, it seems to vary for other span heights. Figure 25 depicts the isentropic Mach number distribution for *0.2* and *0.8* of the span for the cascade with the smallest hub-to-tip ratio. It is visible that the flow is asymmetric for other span heights of the blade row. The biggest differences are noticeable at the suction side of the blade. The fluid near the hub proves to move slower in comparison to the zone near the shroud. However, a remarkably large acceleration takes place in the region close to the trailing edge near the shroud. The acceleration is followed by a diffusion. It was checked that there is no flow separation on the walls of the blades. Such flow asymmetry is expected to influence the flow features downstream of the cascades that will be investigated further in this chapter. Cascade K_E as the most extreme hub-to-tip ratio has been chosen as an exemplary case. The asymmetric effects are expected to be correspondingly less extensive for the bigger hub-to-tip ratios.

6.3 Pressure Gradient in the Blade Passage

In linear cascades, only the blades turn the flow. It results in a higher pressure on the pressure side and a lower pressure on the suction side of a blade. As far as annular cascades are concerned, the flow is turned not only by the blades, but also by the endwalls.

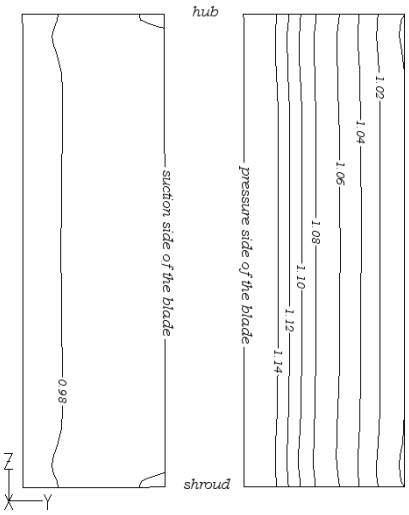

***Figure 26** - Pressure contours [bar] at 0.9b of the linear cascade.*

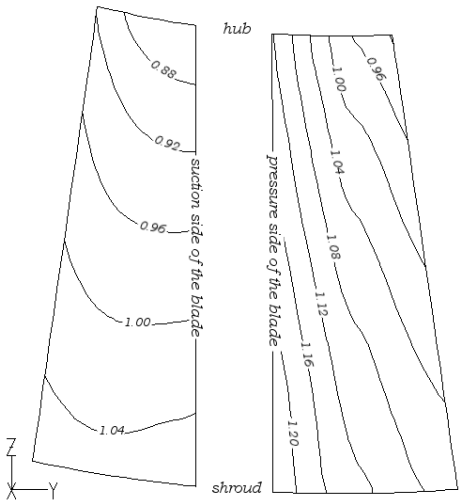

***Figure 27** - Pressure contours [bar] at 0.9b of the cascade K_E.*

The static pressure was investigated in the blade passages of the cascades of two extreme hub-to-tip ratios, namely the linear cascade and the cascade K_E. For this purpose a plane was placed perpendicularly to the *X*-axis at the distance *0.9b* from the leading edge, where most of the turning had taken place. The pressure contours that were collected on this plane are presented in Figure 26 and Figure 27.

A horizontal pressure gradient from the suction side to the pressure side is apparent in the linear cascade. As far as the cascade K_E is concerned, the high pressure on the shroud, which is a consequence of the turning by the endwalls, superposes the high pressure on the pressure side. By the reason of that, a high pressure appears in the area close to the shroud - pressure side corner. The low pressure on the hub side additionally weakens the low pressure on the suction side. It results in a minimal peak of the pressure at the hub - suction side corner. It can be seen that pressure gradient is no longer horizontal and is directed form the hub - suction side corner to the shroud - pressure side corner.

6.4 Outlet Mass Flux Distribution

The outlet mass flux was calculated as a product of the density and the *X*-velocity on the measuring plane. Subsequently, it was pitchwise area averaged for different span values.

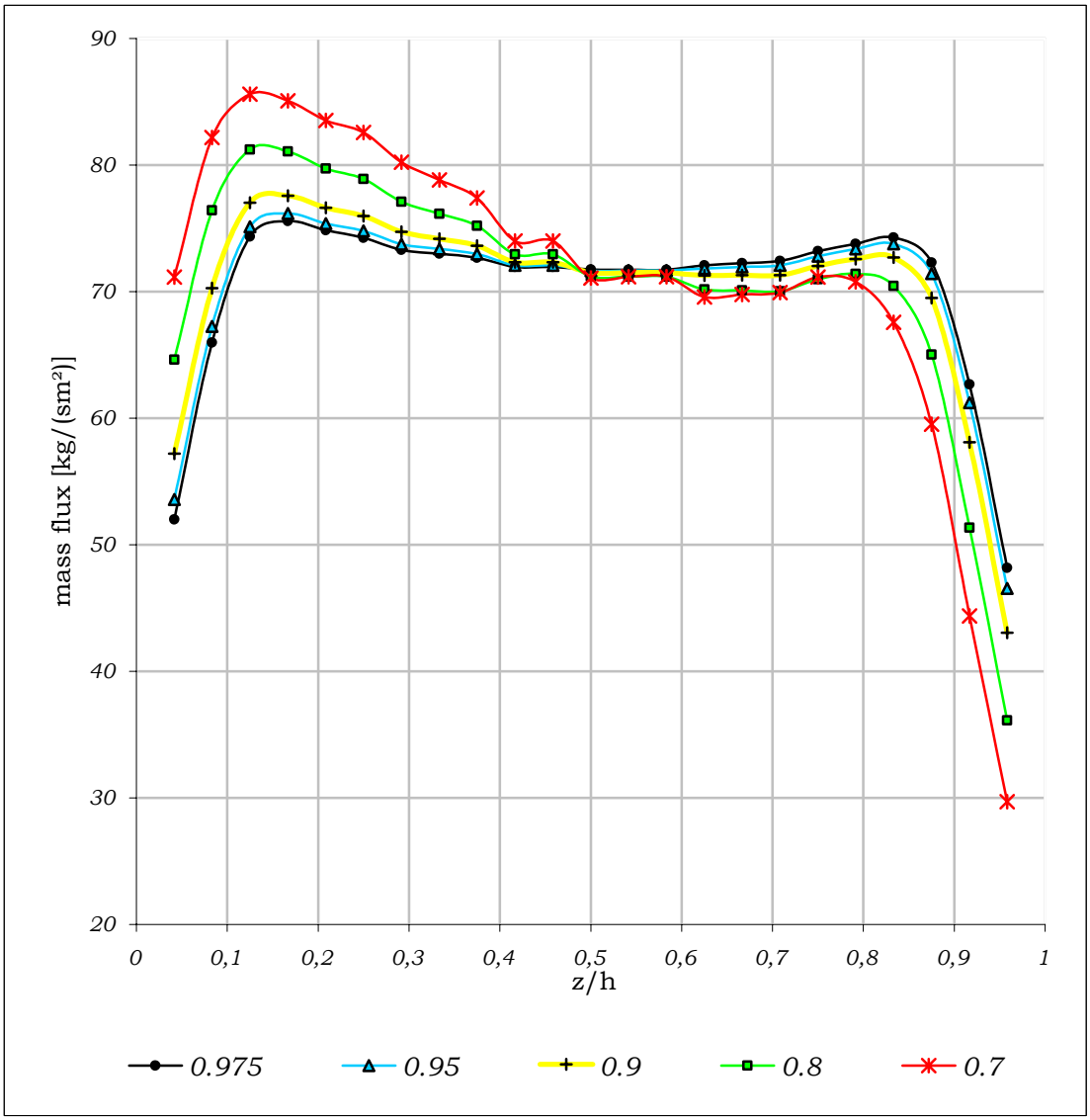

Figure 28 *– Pitchwise area averaged mass flux versus relative blade height.*

It can be noticed in Figure 28 that for decreasing hub-to-tip ratios, the mass flux rises on the hub side of the cascade. The peak mass flux of the cascade K_E, which is at $z/h \approx 0.15$, is by above *10%* higher than the peak of the mass flux in the cascade K_A. On the shroud side, the situation is opposite; the mass flux diminishes for decreasing hub-to-tip ratios. Since the density is nearly constant the outlet mass flux distribution can be treated also as an approximate axial velocity distribution.

6.5 Outlet Circumferential Velocity Distribution

The circumferential velocity was acquired from the vector sum of the *Y*-velocity and the *Z*-velocity that were projected onto the circumferential direction. It was pitchwise averaged for various span heights. The result is exhibited in Figure 29.

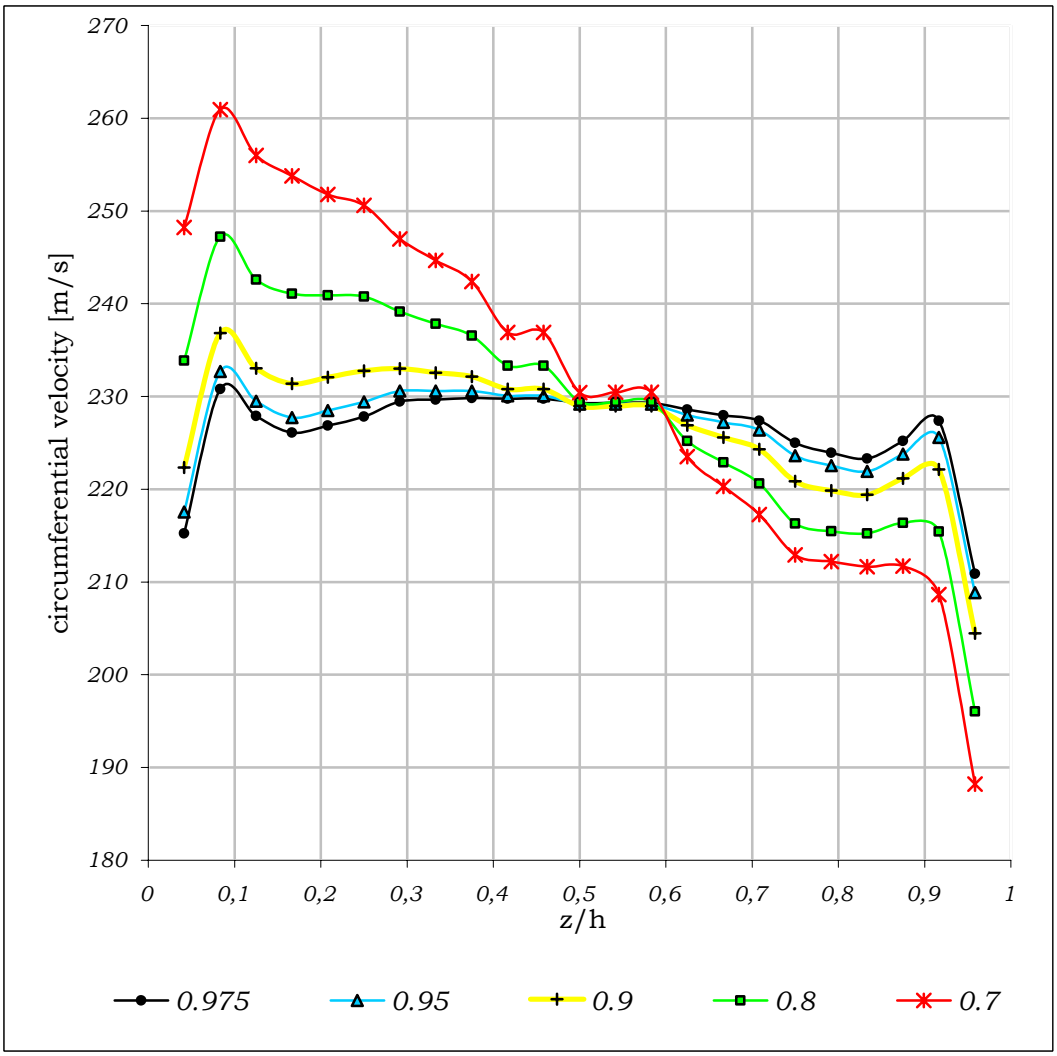

Figure 29 *– Pitchwise area averaged circumferential velocity versus relative blade height*

Some small asymmetry is visible already in cascade K_A and K_B. It is seen that for smaller hub-to-tip ratios the circumferential velocity tends to increase near the hub and decrease near the shroud. The difference between the maximal and the minimal circumferential velocity for the smallest hub to tip ratio (excluding the area of boundary layer) is equal approximately to $50\ m/s$.

It is visible that the circumferential velocity that was used for the outlet pressure calculation is not constant. Especially for smaller hub to tip ratios the variation of the circumferential velocity should be taken into account to obtain a more exact profile of the outlet pressure.

6.6 Outlet Flow Angle Mass Averaged Results

The outlet flow angle was examined on the measuring plane. Figure 30 represents two trends: the area averaged outlet flow angle measured at the midspan and the mass averaged outlet flow angle for the complete measuring plane. It is seen that the area averaged outlet flow angle at midspan rises slightly for growing hub-to-tip ratios. In contrast, it can be noticed that the general tendency of the mass averaged outlet flow angle is to decrease for increasing hub-to-tip ratios. The changes, however, are insignificant and reach at most the difference of about *0.3*° for two extreme hub-to-tip ratios. Owing to that fact the average outlet flow angle could be claimed to be virtually insensitive to the hub-to-tip ratio.

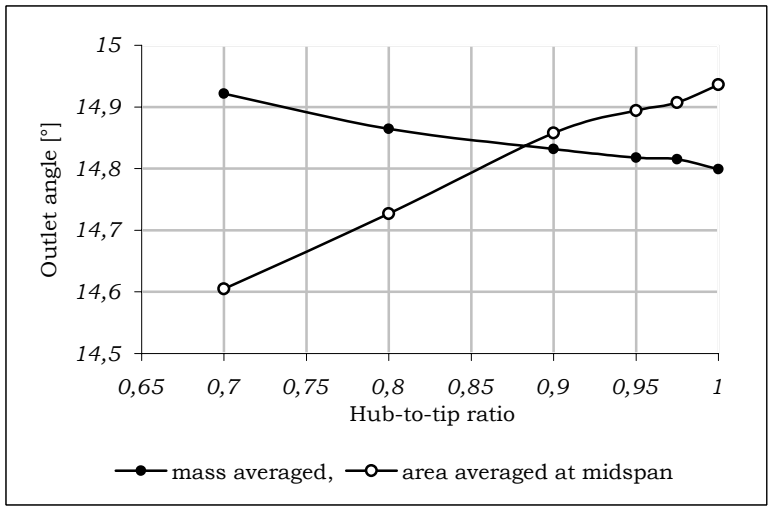

Figure 30 *– Averaged outlet angles versus hub-to-tip ratio*

Due to the asymmetry of the flow that has been mentioned in the Chapter 6.1 and due to the turning of the endwalls mentioned in Chapter 6.3, the outlet flow angle is expected to vary along the span for different hub-to-tip ratios. The outlet flow angle was pitchwise area averaged. The deviation of the outlet angle at particular span height was found by means of Equation (5.4).

As it is visible in Figure 31, the general tendency is that the flow is underturned near the hub and overturned near the casing as the hub-to-tip ratio diminishes. In case of the smallest hub-to-tip ratio, the overturning outflow angle, i.e. $\Delta\beta_2 > 0$, disappears completely in the region of $z/h<0.5$. The difference between the maximal and the minimal outlet angle for the linear cascade is about $4.5°$, while for the smallest hub-to-tip ratio it is approximately $10°$. The outflow angle of the cascades K_A and K_B remains virtually unaffected by the annularity of the row. It appears that the region between the $z/h = 0.5$ and $z/h = 0.8$ is only very little sensitive to the hub-to-tip ratio changes and is very similar for all cascades.

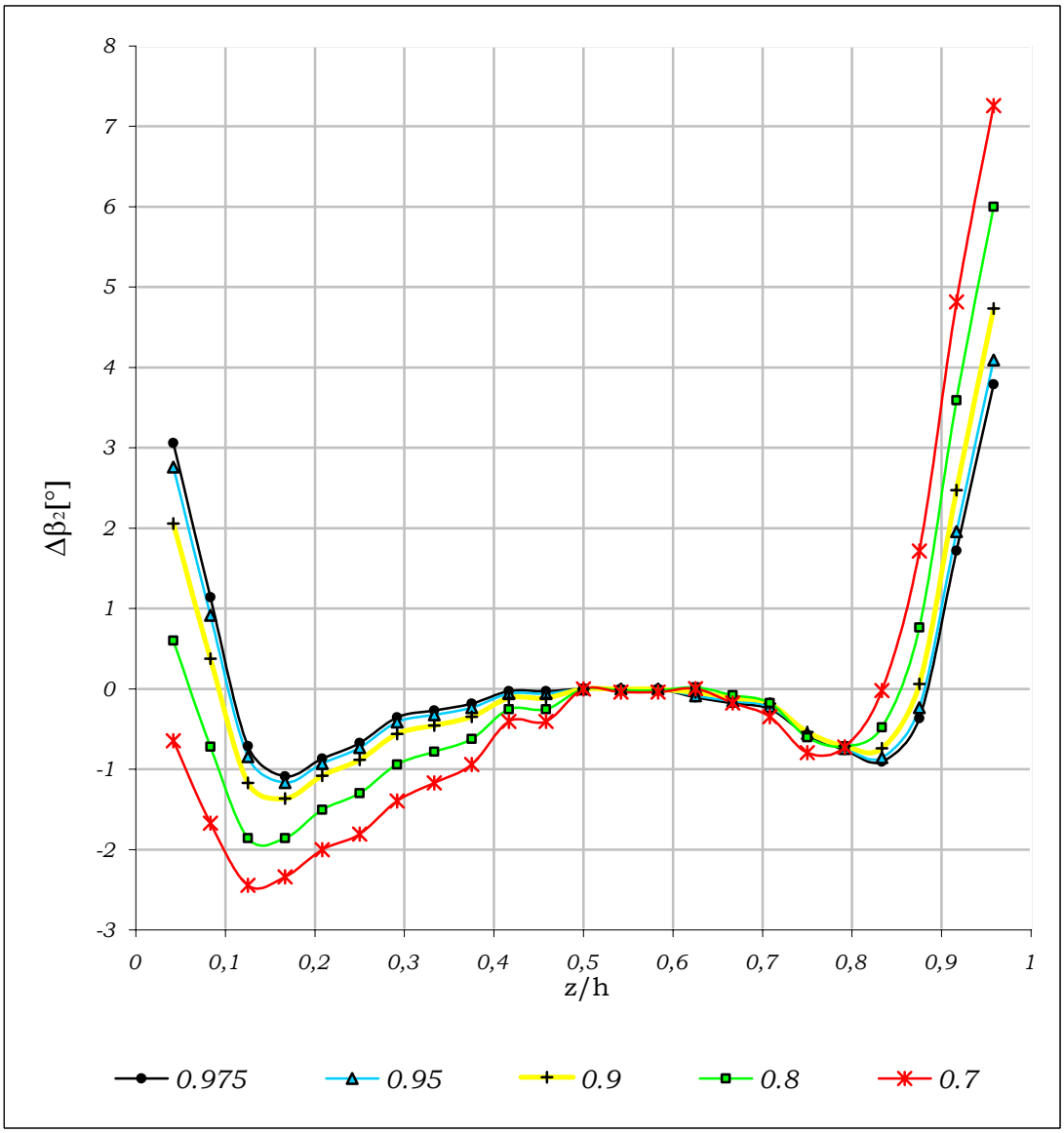

Figure 31 *– Pitchwise area averaged outlet angle deviations versus relative blade height.*

The form of the actual outlet flow angle in the CFD simulation is opposite to the form of the outlet flow angle expected from Equation (3.6); in the results of the CFD simulation, the outlet flow angles for the increasing hub-to-tip ratio are larger near the hub (underturning) than near the shroud (overturning). It was found from Equation (3.6) that the outlet angle for the growing hub-to-tip ratio would be increased near the shroud due to the large o/s and decreased near the hub due to the small o/s.

The outlet angle is not only influenced by the throat opening and the pitch but also, prevailingly, by the secondary flows. At the same time, the usage of the Equation (3.6) to derive a detailed outlet pressure profile from the radial equilibrium condition is open to dispute.

It is author's opinion that such behaviour of the outlet flow angle is caused by the turning of the endwalls and of the blades. It can be deduced from the contour plots of the streamwise vorticity presented in Chapter 6.8 and from Chapter 6.9 where plots of secondary velocity vectors are exhibited. It can be seen there that a relatively large vortex of the positive vorticity is existent on the measuring plane and that the regions of the positive vorticity start to prevail for the decreasing hub-to-tip ratios. Since the azimuthal components of the secondary velocity vectors near the hub side have the opposite sense with respect to the Y-axis sense, the outlet flow angle β_2 is increased (underturning). The azimuthal components of the secondary velocity vectors near the shroud side have the same sense as the Y-axis, resulting in decrease of the outlet flow angle β_2 (overturning).

6.7 Contours of LKEL

Figures 32 to 37 present the LKEL contour plots on the measuring plane. The loss was expressed in percents. There are eight levels of the contours ranging form *0* to *16* for each figure.

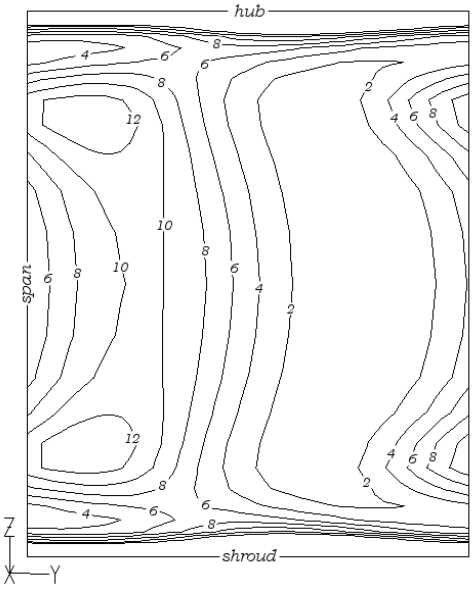

Figure 32 *- Percentage of LKEL of the linear cascade.*

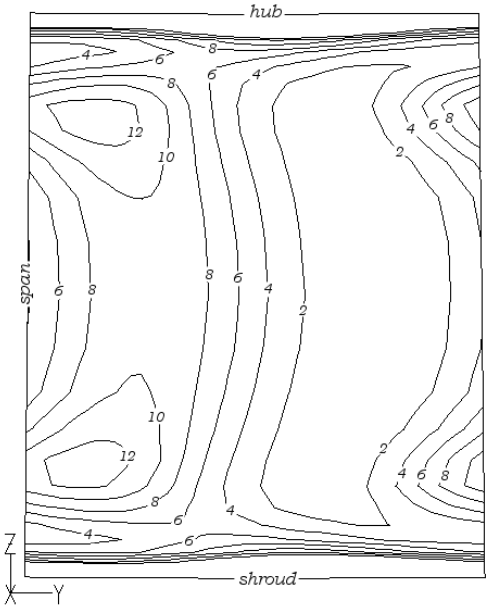

Figure 33 *- Percentage of LKEL of the cascade K_A.*

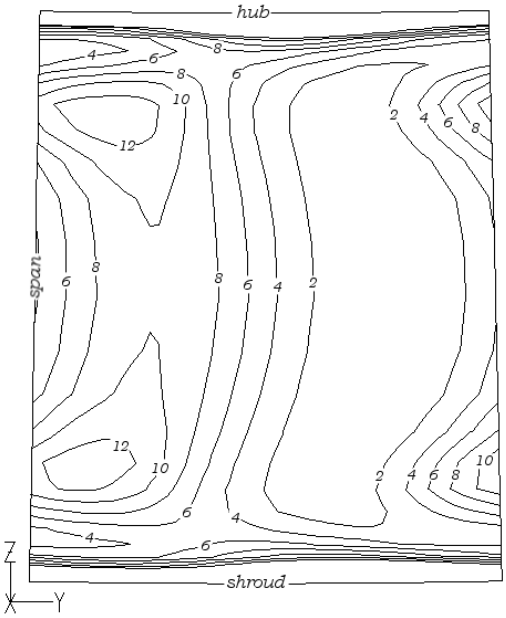

Figure 34 *- Percentage of LKEL of the cascade K_B.*

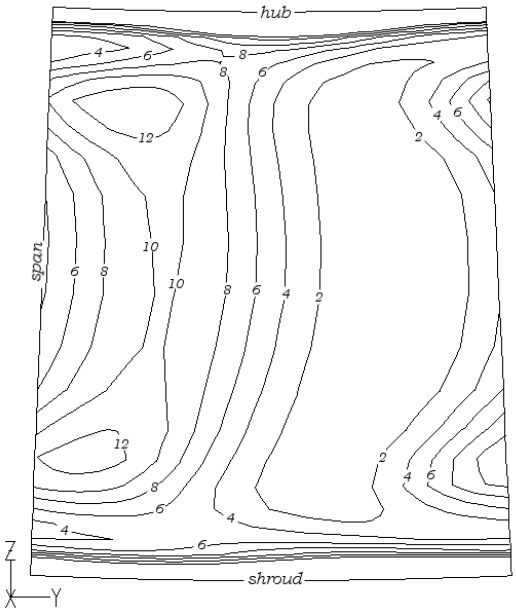

Figure 35 *- Percentage of LKEL of the cascade K_C.*

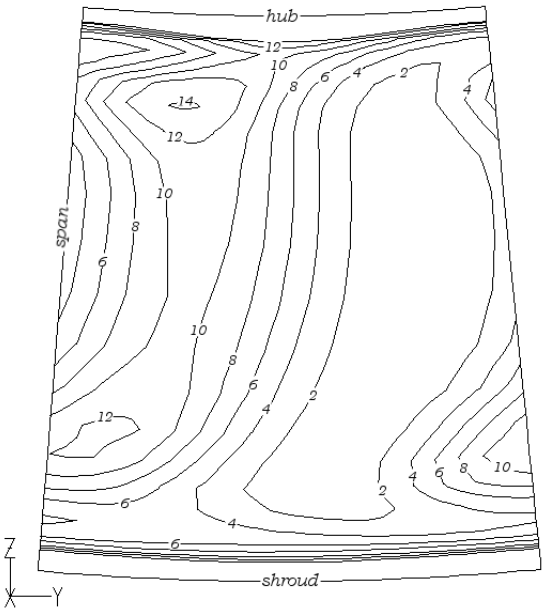

***Figure 36**- Percentage of LKEL of the cascade K_D.*

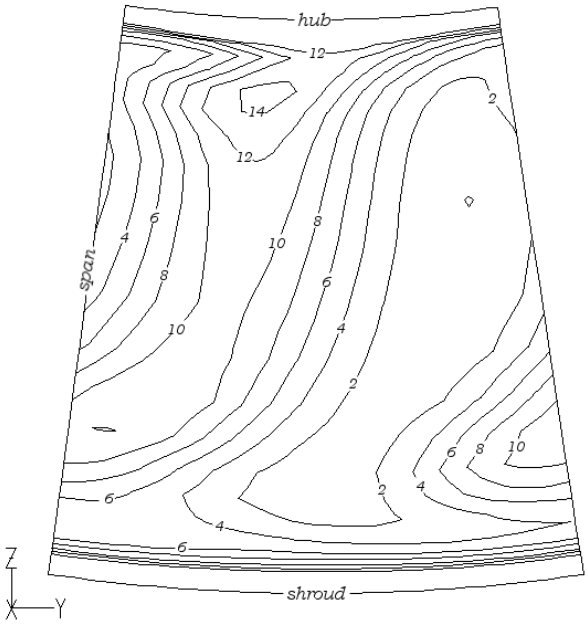

***Figure 37**- Percentage of LKEL of the cascade K_E.*

A typical form of the losses is observable in the flow downstream of the linear cascade. The wake area, which is characterised by a high loss, is swept towards the suction side [1]. Two cores having a loss that reaches *12%* are existent in this zone. Area of the loss below *2%* is associated with the free stream of the flow.

The symmetry and pattern of the losses of linear cascade are scarcely changed for the cascade K_A and K_B. The loss in the area between the loss core and the boundary layer undergoes a small reduction near the shroud (maximum ≈ *6%*) in comparison with the area near the hub (maximum ≈ *8%*). The loss of the wake in the area of midspan diminishes from *10%* to *8%* with respect to the linear cascade. It can result in a slightly reduced midspan loss for these two cascades.

In the flow of the cascade K_C a further tendency for reducing losses near the shroud and for increasing the losses near the hub is noticeable.

Distinct asymmetry is visible in the form of LKEL in the cascades K_D and K_E. The loss core near the hub in comparison with the one near the shroud is shifted to the suction side. The peak value of the core near the hub reaches *14%* and a high loss area is visible around this point. Near the casing, the loss fades and the loss core nearly disappears for the cascade K_E.

6.8 Streamwise Vorticity Contours

Vorticity contours were drawn on the measuring plane. There are ten levels in the range from *–10* to *10*. The regions having a negative vorticity (clockwise rotation) were coloured with grey for clarity. The vorticity was "nondimensionalised" by means of the free stream velocity and the chord of the blade [1].

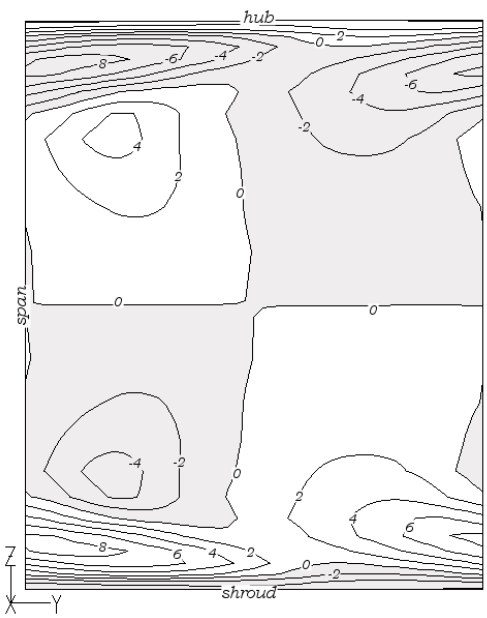

Figure 38 *- Dimensionless vorticity of the linear cascade.*

Figure 39*- Dimensionless vorticity of the cascade K_A .*

Figure 40 *- Dimensionless vorticity of the cascade K_B .*

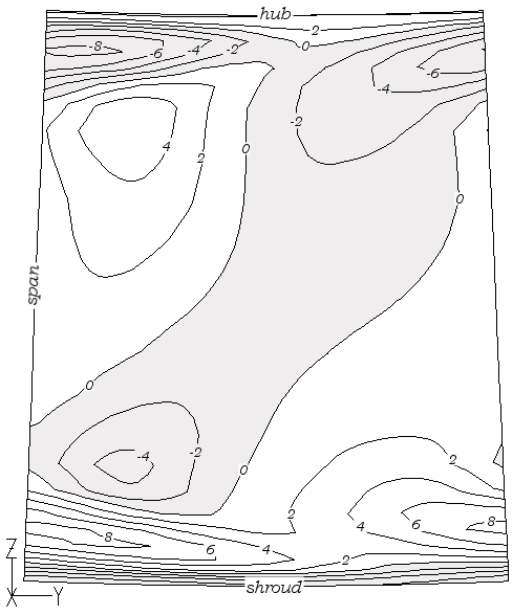

Figure 41 *- Dimensionless vorticity of the cascade K_C .*

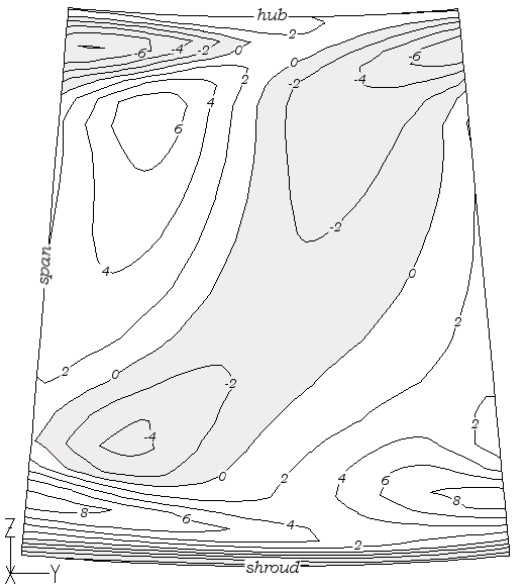

Figure 42 *- Dimensionless vorticity of the cascade K_D .*

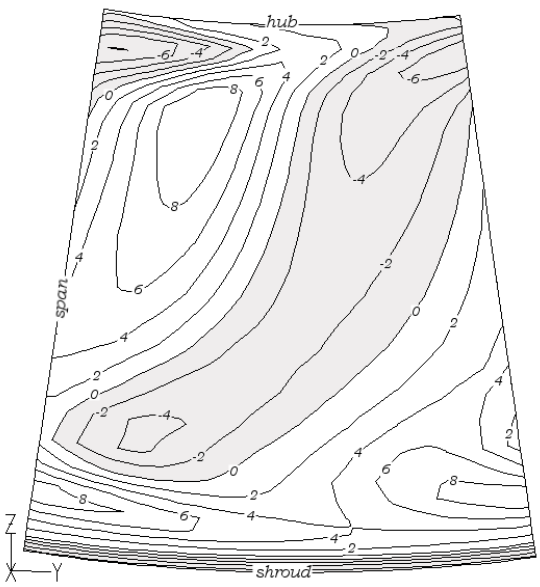

Figure 43 *- Dimensionless vorticit. of the cascade K_E .*

As for the linear cascade, two peaks of the vorticities near both hub and shroud can be seen. The peak value *±4* in the area of the wake can be associated with the shed vortex. The passage vortex vorticity reaches the value of *±8*. An increasing vorticity in the direction of the endwalls could be associated with the corner vortex, although its appearance in this CFD simulation should not be taken for granted.

For the cascades K_A and K_B, some asymmetry effects are already noticeable. Some vorticity levels having values different than zero appear near the midspan. However, no change in the peak values can be seen.

In case of the cascade K_C, the area of the positive vorticity grows. The area around the positive peak near the hub is more extensive than that one near the shroud.

For the cascades K_D and K_E, the dominance of the positive vorticity is clearly visible. The peak value of the positive vorticity near the hub rises gradually and achieves the value of *8* for the smallest hub-to-tip ratio. The level of the maximal and the minimal vorticities near the shroud remains roughly the same for all cascades.

The dominance of the positive vorticity for the cascades having the smaller hub-to-tip ratio means that the fluid generally tends to rotate in the counter clockwise direction on the measuring plane of those cascades.

6.9 Plots of Secondary Velocity Vectors

Figure 44 represents the secondary flows in a curved rectangular channel. It can be seen that the flow is swept inward near the endwalls (walls *g* and *d*) and outward in the middle of the channel. The secondary flows are caused by the interaction between the boundary layers and the pressure field that results from the centrifugal acceleration. The pressure gradient that appears due to the turning is not balanced by the reduced velocity in the boundary layers, which pushes the flow in the boundary layers near the walls in the inward direction. Owing to the mass conservation rule, the flow is constrained to move outward in the middle of the channel [21]. This situation can be associated with the flow through annular cascades. It can be noticed in the figures representing secondary flows in the annular cascades that the flow is swept outward, i.e. in the shroud direction, in the free stream area. The wake area, which is made of the boundary layers from the blade walls, is characterised by the inward secondary flow, i.e. in the hub direction.

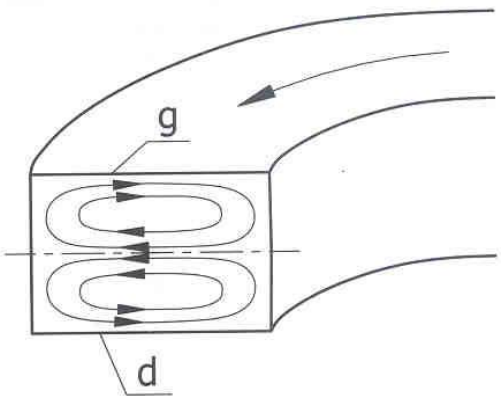

***Figure 44** – Secondary flows in a curved rectangular channel [12].*

The vortices produced by the turning of the endwalls interact with the passage vortices, which are induced by turning of the blades, and shed vortices. The interaction results in the typical form of secondary flows downstream of annular cascades.

The secondary velocity vectors are depicted in Figures 45 to 50. The vectors were drawn on the measuring plane. The vector of the length *10 m/s* is attached to each figure so that the magnitude of the secondary velocities can be compared. For clarity, vortices were denoted with grey arrows. *"P"* indicates an area that could be associated with a passage vortex. *"S"* refers to a shed vortex.

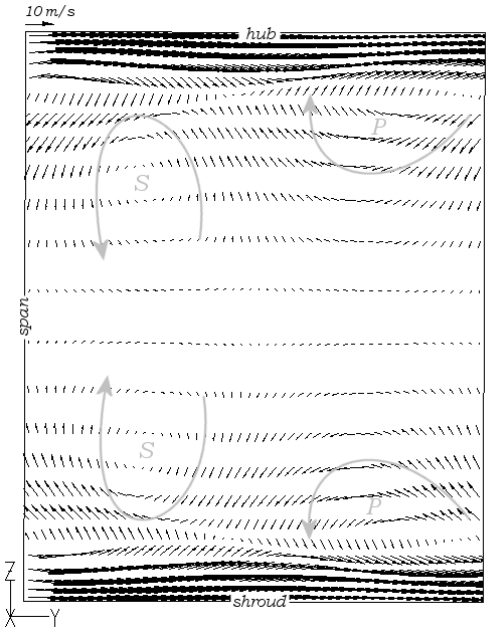

***Figure 45** - Secondary velocity vectors of the linear cascade.*

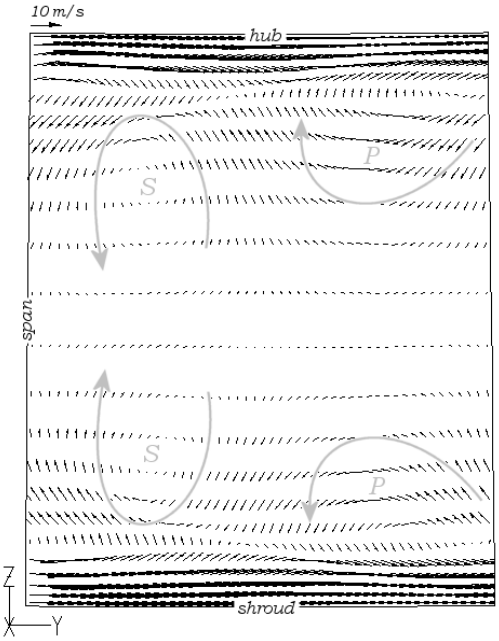

***Figure 46** - Secondary velocity vectors of the cascade $K_{A.}$*

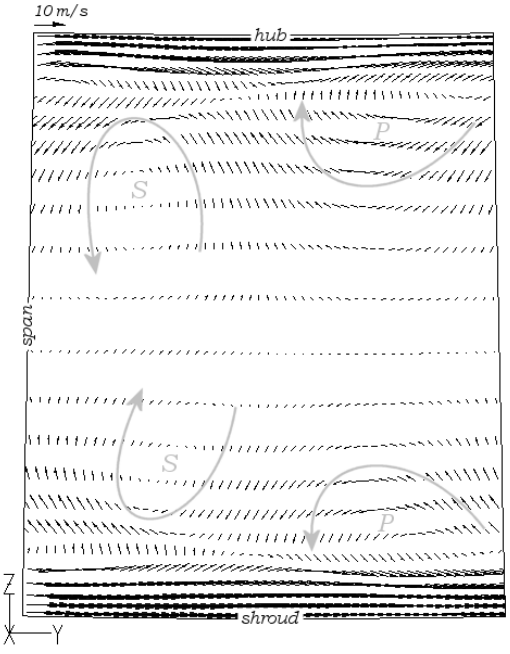

***Figure 47** - Secondary velocity vector of the cascade $K_{B..}$*

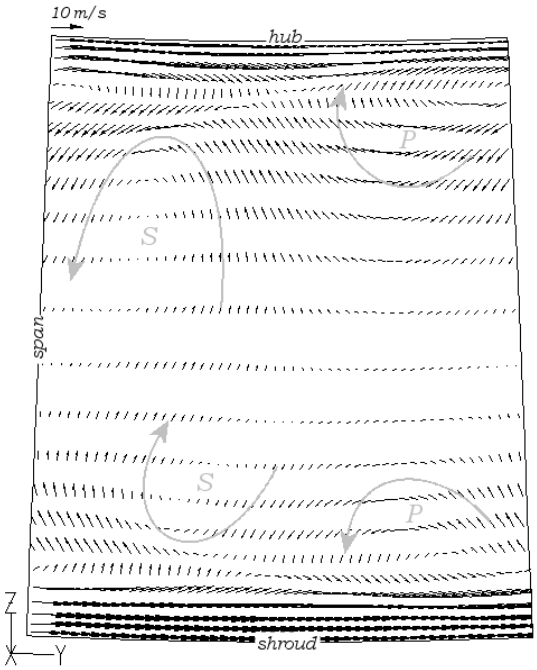

***Figure 48**- Secondary velocity vectors of the cascade $K_{C.}$*

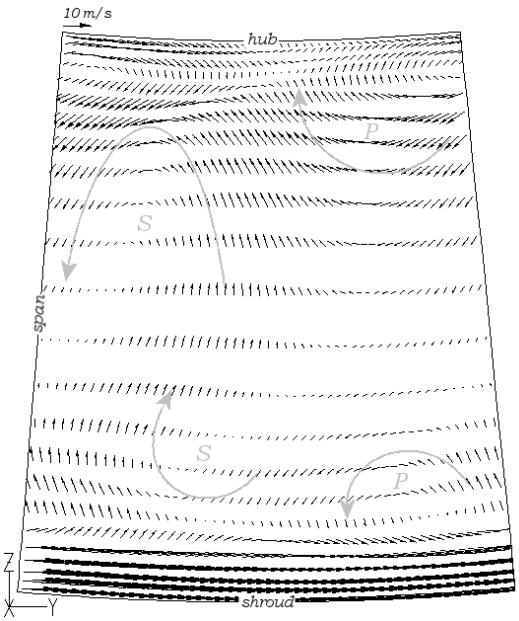

***Figure 49** - Secondary velocity vectors of the cascade K_D.*

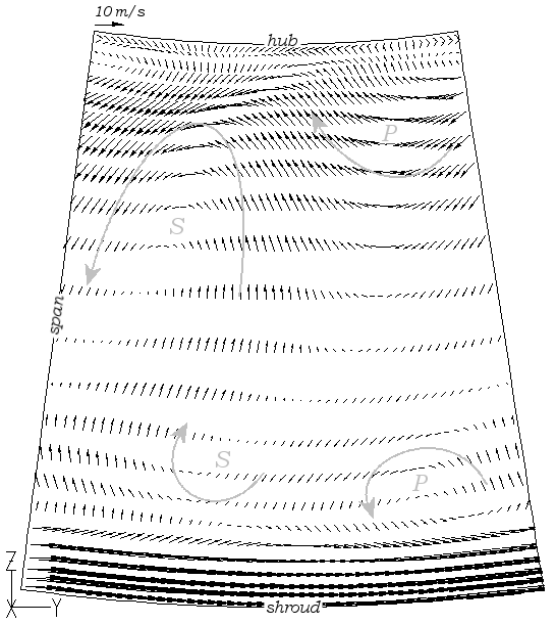

***Figure 50** - Secondary velocity vectors of the cascade K_E.*

The downstream flow of the linear cascade produces a typical vortex structure; a pair of shed and a pair of passage vortices are visible. There are no clear traces of the suction side of the horseshoe vortex [1]. The pressure side of the horseshoe vortex seems to prevail in the creation of the passage vortex.

The symmetry of the vortex structure is preserved in the flow downstream of the cascades K_A and K_B. Only very small influence of the annularity is noticeable. The shed vortex near the shroud of the cascades K_B and K_C moves in the direction of the suction side cascade. It starts to contribute to the shed vortex on the hub side. Noticeable radial flow appears from shroud to hub. This flow is driven in the wake area.

The mentioned radial flow is considerably stronger downstream of the cascade K_D. The vortices near the hub are more intensive with respect to those near the shroud. The strength of the passage vortex near the shroud undergoes a reduction.

The intensity of the vortices experiences further weakening near the shroud of the cascade K_E. The shed vortex near the hub appears to be much stronger than the other vortices. Strong radial flow in the direction of the hub is visible in the area of the trailing edge wake. The radial flow in the area associated with the free stream is driven in the direction of the shroud.

6.10 Mass & Area Averaged Results of the Losses

Mass averaged results of total and secondary losses are shown in Figure 51. Losses were calculated in FLUENT by means of the methods described in Chapter 5.7.

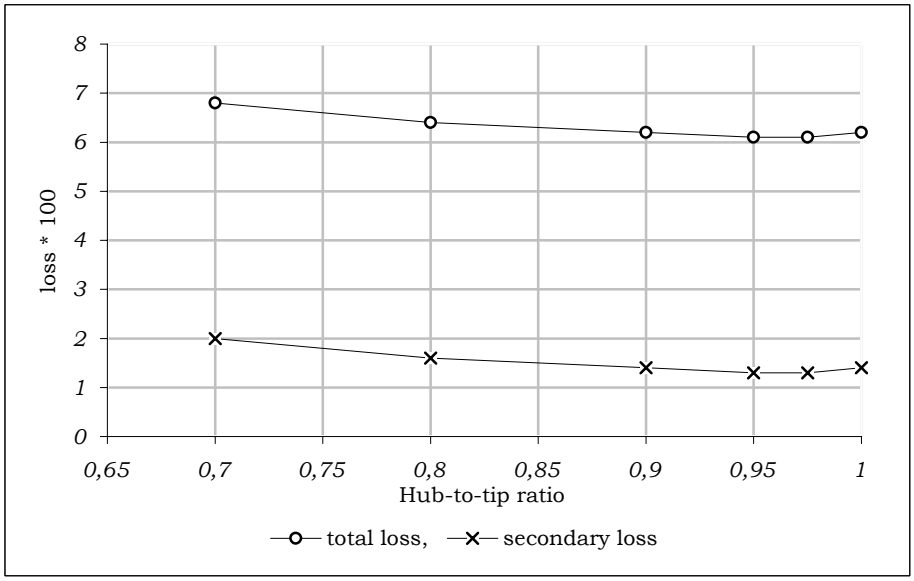

***Figure 51** - Mass averaged losses*

Midspan loss of the linear cascade was treated as a representative of the profile loss for all the cascades. It was difficult to separate the profile loss from the total loss of the annular cascades due to the three-dimensional flow that exists near the midspan. The mass averaging of the losses at the midspan of the linear cascade resulted in the profile loss equal to *4.8%*.

A small reduction of the secondary loss is visible for the cascades K_A and K_B with respect to the linear cascade. It can be caused by the phenomena described in [7]. The walls of the blades are inclined to the hub wall and to the shroud wall in such a way that they introduce additional pressure gradients which tend to reduce the secondary effects. On the other hand, it can be caused also by inaccuracies introduced by the CFD method.

For the rest of the cascades, the secondary loss increases little by little with the decreasing hub-to-tip ratios. However, it can be seen that the annularity of the cascades does not cause large changes in the averaged secondary loss.

It can be caused by the fact that the high loss near the hub is counterbalanced by the reduced loss near the shroud for the lower hub-to-tip ratios.

Due to the increasing secondary loss, the total loss rises as well. The lowest total loss equal to *6.1%* appears in the cascades K_A and K_B. The highest total loss, which is for the cascade K_E, is equal to *6.8%*.

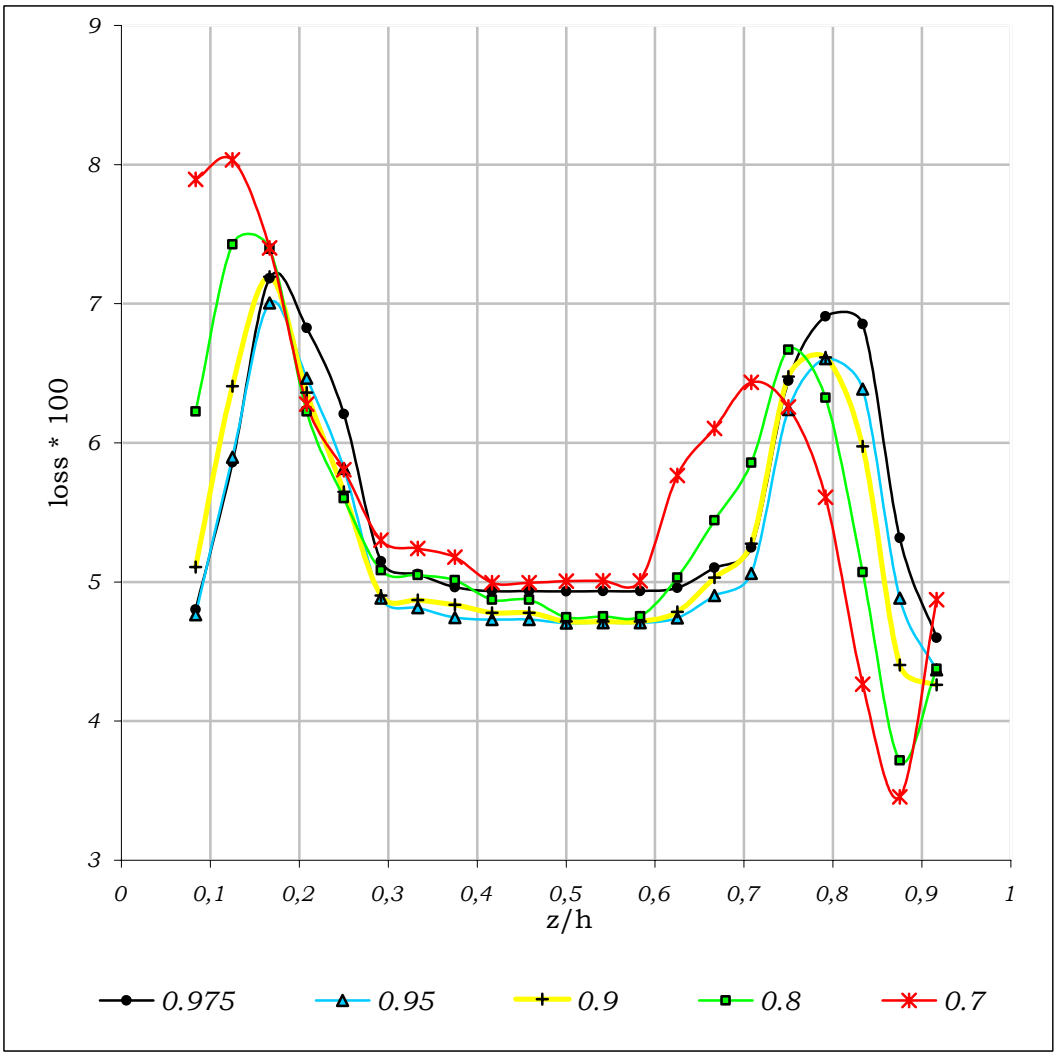

Figure 52 *– Pitchwise area averaged total losses versus relative blade height*

Figure 52 exhibits the pitchwise area averaged total losses for different relative blade heights. The losses close to the endwalls were omitted. An area of relatively constant total loss can be seen between $z/h \approx 0.4$ and $z/h \approx 0.6$. The loss induced by the secondary effects is seen for other relative blade heights. The total loss near the hub tends to grow while the total loss near the shroud tends to diminish for decreasing hub-to-tip ratios.

7 Conclusions

The flow was simulated by means of Computational Fluid Dynamics in a linear cascade and five annular cascades having hub-to-tip ratios equal to *0.975, 0.95, 0.9, 0.8* and *0.7*. The cascades' blade profile was derived from a stator of a high-pressure turbine. Annular cascades were constructed in such a manner that the trailing edges were stacked radially and the pitch at the mean radius was equal to the linear cascade's pitch.

The flow was examined using profile Mach number distributions, contours of downstream axial velocity, pressure contours in the blade passage, mass flux distribution, circumferential velocity distribution, outlet angle, local kinetic energy loss, contours of vorticity as well as secondary velocity vectors and losses.

It was found that for the decreasing hub-to-tip ratio:

- The loss near the hub increases while it decreases near the shroud.
- The secondary flows near the hub strengthen whereas they weaken near the shroud. The secondary flow commences to move across the midspan. The radial flow in the wake area is driven in the direction of the hub. As far as the radial flow in the free stream area is concerned it migrates in the direction of the shroud.
- The peak value of the positive vorticity near the hub rises. The area of the positive vorticity grows.
- The flow is underturned near the hub and overturned near the shroud.

The following factors are suspected to be the reasons for such flow behaviour:

- Flow turning by the endwalls.
- Interaction between additional pressure gradient in the blade passage, which is caused by the turning of the endwalls, and the boundary layers.
- Various angles between endwalls and blades' surfaces.
- Different incidence conditions.

Moreover, it was observed that it is difficult to obtain a realistic spanwise distribution of the outlet angle from the simplified sine rule. It appears that the outlet angle was greatly influenced by the secondary flows in the annular cascades investigated within this work.

8 Bibliography

[1] A. Perdichizzi, V.Dossena: “Incidence Angle and Pitch-Chord Effects on Secondary Flows Downstream of a Turbine Cascade”. ASME Journal of Turbomachinery, Vol. 115, pp 383-391, July 1993.

[2] E. Tuliszka: “Turbiny Cieplne – Zagadnienia Termodynamiczne i Przeplywowe”, Warszawa 1973.

[3] K.J.Müller, R. Willinger, H. Haselbacher: „Grundzüge der Thermischen Turbomaschinen“, Skriptum zur Vorlesung, Institut für Thermodynamik und Energiewandlung, Technische Universität Wien, 2001.

[4] Fluent 6.0 Documentation.

[5] Gambit 2.1 Documentation.

[6] Z. Kazimierski, Z. Orzechowski: “Mechanika Płynów”, Politechnika Łódzka, 1993.

[7] F. Wingelhofer: „Neue Kriterien zur Auslegung dreidimensionaler Beschaufelungen von Axialturbinen.”, PhD thesis, Institut für Thermodynamik und Energiewandlung, Technische Universität Wien, 2003.

[8] A. Yamamoto, F. Mimura, J. Tominaga, S. Tomihisa, E. Outa and M. Matsuki: “Unsteady Three-Dimensional Flow Behavior Due to Rotor-Stator Interaction in an Axial-Flow Turbine”, ASME 93-GT-404, May 1993.

[9] J.D. Denton: “Loss Mechanisms in Turbomachines”. ASME Journal of Turbomachinery, Vol. 115, pp 621-656, October 1993.

[10] Site: http://mathworld.wolfram.com

[11] K.Bammert, H.Kläukens: "Nabentotwasser hinter Leiträdern von axialen Strömungsmaschinen". Ingenieur-Archiv. XVII. Band, 1949.

[12] Z. Kazimierski: „ Podstawy Mechaniki Płynów i Metod Komputerowej Symulacji Przepływów", Politechnika Łódzka, 2004.

[13] A. Perdichizzi: „Mach Number Effects on Secondary Flow Development Downstream of a Turbine Cascade". ASME Journal of Turbomachinery, Vol. 112, pp 643-651, October 1990.

[14] H.P. Wang, S.J. Olson, R.J. Goldstein, E.R.G. Eckert: „Flow Visualization in a Linear Turbine Cascade of High Performance Turbine Blades". ASME Journal of Turbomachinery, Vol. 119, pp 1-8, January 1997.

[15] M.T Schobeiri, J.L. Gilarranz, E.S. Johansen: „Aerodynamic and Performance Studies of a Three-Stage High Pressure Research Turbine with 3-D Blades, Design Point and Off-Design Experimental Investigations". Proceedings of ASME TURBOEXPO 2000, ASME 2000-GT-484, Munich Germany, May 2000.

[16] H.E. Gallus, J. Zeschky, C. Hah: "Endwall and Unsteady Flow Phenomena in an Axial Turbine Stage". ASME 94-GT-143, June 1994.

[17] V.S.P. Chaluvadi, A.I. Kalfas, M.R. Banieghbal, H.P. Hodson J.D. Denton: "Blade-Row Interaction in a High-Pressure Turbine". Journal of Propulsion and Power, Vol. 17, No.4, pp 892-901, July-August 2001.

[18] R.P. Dring, H.D. Jolsyn, L.W. Hardin, J.H. Wagner: "Turbine Rotor-Stator Interaction". ASME 82-GT-3, June 1982.

[19] P. Lampart: "Numerical Optimisation of a High Pressure Steam Turbine Stage". Conference on Modeling Fluid Flow, The 12th International Conference on Fluid Flow Technologies, Budapest, Hungary, September 2003.

[20] D. Jolsyn, R Dring: "Three-Dimensional Flow in an Axial Turbine: Part 1- Aerodynamic Mechanisms". ASME Journal of Turbomachinery, Vol. 114, pp 61-70, January 1992.

[21] B. Eck: "Technische Strömungslehre, Band 2: Anwendungen". Springer-Verlag, Berlin Heidelberg New York, 1981.

[22] „VDI-Wärmeatlas: Berechnungsblätter für den Wärmeübergang. Verein Deutscher Ingenieure, VDI-Gesellschaft Verfahrenstechnik und Chemieingenieurwesen (GVC), 7. erweiterte Auflage", VDI-Verlag, Düsseldorf,1994.

Appendix A

The examples of the user-defined functions that were required for the pre- and the postprocessing of the CFD simulation are presented within this appendix. The standard C compiler provided in UNIX was used to compile the programs. Subsequently, the UDF libraries were linked to the FLUENT process at runtime [4]. Examples of the programs are given only for the cascade K_A.

a) The *Y*-velocity component at the inlet.

Description: it is a "define profile" macro type that is usually used to define custom boundary profiles. After linking, the macro is available in the boundary condition menus in FLUENT. The macro loops over the face checking coordinates of the cell and calculating the velocity component in the *Y*-direction with the help of Equation (3.18).

Code:

```
#include "udf.h"
DEFINE_PROFILE(inlet_yvel_comp, thread, value)
{
  face_t inlet_face;

  const real comp = -0.2402;

  real x[ND_ND];
  real r_y;
  real r_z;

        begin_f_loop(inlet_face, thread)
        {
                F_CENTROID(x, inlet_face, thread);

                r_y = x[1];
                r_z = x[2];

                F_PROFILE(inlet_face, thread, value) = - comp * r_z / pow(pow(r_y,2) + ..
                                                                        ..pow(r_z,2), 0.5);

        }
        end_f_loop(inlet_face, thread)
}
```

b) The *Z*-velocity component at the inlet.

Description: it is the same macro type as for the *Y*-velocity component. The component in the *Z*-direction is calculated with the help of Equation (3.19).

Code:

```
#include "udf.h"
DEFINE_PROFILE(inlet_zvel_comp, thread, value)
{
  face_t inlet_face;

  const real comp = -0.2402;

  real x[ND_ND];
  real r_y;
  real r_z;

        begin_f_loop(inlet_face, thread)
        {
                F_CENTROID(x, inlet_face, thread);

                r_y = x[1];
                r_z = x[2];

                        F_PROFILE(inlet_face, thread, value) = - comp * r_z / pow(pow(r_y,2) + ..
                                                                        ..pow(r_z,2), 0.5);

        }
        end_f_loop(inlet_face, thread)
}
```

c) The inlet boundary layer

Description: it is the same macro type as for the *Y*-velocity component. The span distance of the cell is calculated and corresponding value of mass flux is obtained from Equations (3.13) and (3.22).

Code:

```
#include "udf.h"
DEFINE_PROFILE(inlet_mass_flux_Ra, thread, value)
{
  face_t inlet_face;

  const real exp=0.166666;
  const real ra=1.950141;
  const real flux=78.19;

  real x[ND_ND];
  real s;
  real r_y;
  real r_z;
  real r;

        begin_f_loop(inlet_face, thread)
        {
                F_CENTROID(x, inlet_face, thread);

                r_y = x[1];
                r_z = x[2];
                r = pow(pow(r_y,2) + pow(r_z,2), 0.5);
                s = r - ra;

                if (s<0.0203)
                  F_PROFILE(inlet_face, thread, value) = flux * pow(s/0.0203,exp);
                else if ((s>=0.0203) && (s<=0.0297))
                  F_PROFILE(inlet_face, thread, value) = flux;
                else if (s>0.0297)
                  F_PROFILE(inlet_face, thread, value) = flux * pow((0.05-s)/0.0203,exp);
        }
        end_f_loop(inlet_face, thread)
}
```

d) Outlet pressure profile

Description: it is the same macro type as for the *Y*-velocity component. The span distance of the cell is calculated and the corresponding value of the static pressure is obtained from Equation (3.7).

Code:

```
#include "udf.h"
DEFINE_PROFILE(simple_outlet_p_Ra, thread, value)
{
  face_t outlet_face;

  const real rm = 1.975299;
  const real average_pressure = 101325;
  const real density = 1.162;
  const real y_vel = 218;

  real x[ND_ND];
  real r_y;
  real r_z;
  real r;

        begin_f_loop(outlet_face, thread)
        {
                F_CENTROID(x, outlet_face, thread);

                r_y = x[1];
                r_z = x[2];
                r = pow(pow(r_y,2) + pow(r_z,2), 0.5);

                F_PROFILE(outlet_face, thread, value) = average_pressure + density * ..
                                                                        ..pow(y_vel,2) * log(r/ rm);

        }
        end_f_loop(outlet_face, thread)
}
```

e) LKEL

Description: it is a "define adjust" macro type. This macro needs to be hooked in FLUENT. Subsequently, the user-defined memory requires to be allocated. The macro runs every time when the simulation is iterated. To obtain the value of the LKEL, it is necessary to input some data of the flow to the code, i.e. the total temperature and the average pressure at the inlet, the average total pressure and the velocity magnitude at the inlet midspan and average static pressure at the outlet midspan. FLUENT offers access through a UDF to only few flow variables. Hence, the total pressure for every cell at the inlet is obtained by means of Equation (8.1). Mach number is calculated from Equation (8.2). The total pressure and the static temperature are assumed to be constant at the inlet.

$$p_t = p \cdot (1 + \frac{\kappa - 1}{2} Ma^2)^{\frac{\kappa}{\kappa - 1}} \qquad (8.1)$$

$$Ma = \frac{\left|\vec{c}_1\right|}{\sqrt{\kappa R T_t - \frac{\left|\vec{c}_1\right|^2 \cdot (\kappa - 1)}{2}}} \qquad (8.2)$$

Code:

```
#include "udf.h"

DEFINE_ADJUST(lkel_Ra,d)
{
        Thread *t;
        cell_t c;
        face_t f;

        const real exp=0.166666;
        const real ra=1.950141;

        const real kappa=1.4;
        const real gas_const=287.04;

        const real c1_MS=54.6;
        const real temptot1=328.79;
        const real av_ps1=138616.5;
        const real av_ps2_MS=101435.9;
        const real av_pt1_MS=140826.5;

 thread_loop_c (t,d)
  {
     {
      begin_c_loop (c,t)
       {
                        real x[ND_ND];
                        real s;
                        real r_y;
                        real r_z;
                        real r;

                        real pt1;
                        real pt2;
                        real ps2;
                        real temp2;

                        real vel1_mag;
                        real Ma1;
                        real x2_vel;
                        real y2_vel;
                        real z2_vel;
                        real vel2_mag;
                        real Ma2;
                        real zeta;

                        C_CENTROID(x, c, t);

                        r_y = x[1];
                        r_z = x[2];
                        r = pow(pow(r_y,2) + pow(r_z,2), 0.5);
                        s = r - ra;

                        if (s<0.0203)
                                vel1_mag = c1_MS * pow(s/0.0203,exp);
                        else if ((s>=0.0203) && (s<=0.0297))
                                vel1_mag = c1_MS;
                        else if (s>0.0297)
                                vel1_mag = c1_MS * pow((0.05-s)/0.0203,exp);

                        Ma1=vel1_mag/pow((kappa*gas_const*temptot1-(kappa-1) ..
                                                        ..*pow(vel1_mag,2)/2),0.5);
                        pt1=av_ps1*pow((1+pow(Ma1,2)*(kappa-1)/2),(kappa/(kappa-1)));

                        ps2=C_P(c,t);
                        temp2=C_T(c,t);

                        x2_vel=C_U(c,t);
                        y2_vel=C_V(c,t);
                        z2_vel=C_W(c,t);
                        vel2_mag=pow((pow(x2_vel,2)+pow(y2_vel,2)+pow(z2_vel,2)),0.5);
                        Ma2=vel2_mag/pow((kappa*gas_const*temp2),0.5);

                        pt2=ps2*pow((1+pow(Ma2,2)*(kappa-1)/2),(kappa/(kappa-1)));

                        zeta=(pow(ps2/pt1,0.4/1.4)-pow(ps2/pt2,0.4/1.4)) ..
                                                .. /(pow(av_ps2_MS/av_pt1_MS,0.4/1.4)-1);
                        C_UDMI(c,t,0) = zeta;
       }
      end_c_loop (c,t)
     }
  }
}
```

Appendix B

The coordinates of the blade profile:

X	*Y*
0	0
0,1266	1,2015
0,5682	2,326
1,2929	3,2927
2,2484	4,0319
3,3661	4,4902
4,587	4,8152
5,7987	5,1725
6,9927	5,5851
8,1684	6,0474
9,3293	6,5455
10,4767	7,0742
11,6063	7,6398
12,7107	8,2531
13,7841	8,9192
14,8237	9,6369
15,829	10,402
16,7993	11,2108
17,7343	12,0603
18,6337	12,9475
19,4976	13,8693
20,3264	14,8226
21,1212	15,8047
21,8828	16,8126
22,6126	17,8438
23,312	18,8959
23,9828	19,9665
24,6268	21,0534
25,8427	23,2681
26,419	24,3924
26,9775	25,5256
27,52	26,6666
28,0475	27,8146
28,5711	28,9689
29,0621	30,1287
29,5518	31,2932
30,0317	32,4619
30,5023	33,6344
30,964	34,8104
31,4169	35,9898
31,8524	37,1724
32,2978	38,358
32,7259	39,5466
33,1472	40,7379

X	*Y*
33,5603	41,9317
33,6002	42,0093
33,6608	42,0721
33,7369	42,1149
33,8221	42,134
33,9091	42,1278
33,9908	42,0968
34,06	42,0437
34,1111	41,9729
34,1397	41,8905
34,1444	41,8031
33,9238	40,598
33,6978	39,3938
33,4659	38,1907
33,229	36,9807
32,9864	35,7878
32,7381	34,588
32,4843	33,3895
32,2249	32,192
31,9601	30,9958
31,69	29,8008
31,4146	28,6069
31,134	27,4143
30,8482	26,2229
30,557	25,0329
30,2599	24,2367
29,9566	22,6572
29,6468	21,4719
29,3299	20,2884
29,0048	19,1071
28,6705	17,9284
28,3259	16,7527
27,9697	15,5805
27,601	14,4121
27,2186	13,2481
26,8216	12,089
26,4087	10,9355
25,9782	9,7885
25,528	8,649
25,0562	7,5184
24,5611	6,3978
24,0418	5,2881
23,4975	4,1904
22,9252	3,1072

X	*Y*
22,3199	2,0421
21,6769	0,9993
20,994	-0,0178
20,2691	-1,0054
19,4964	-1,956
18,6701	-2,8603
17,7952	-3,7179
16,8745	-4,5259
15,8858	-5,2484
14,8302	-5,8659
13,7264	-6,4003
12,572	-6,8085
11,3764	-7,0725
10,1571	-7,1834
8,9339	-7,1322
7,7277	-6,922
6,5566	-6,5646
5,4319	-6,08
4,3598	-5,488
3,344	-4,8037
2,3846	-4,042
1,4855	-3,2103
0,7048	-2,2883
0,1975	-1,1919
0	0